From burial to exhumation: emplacement and metamorphism of mafic eclogitic terranes constrained through multimethod petrochronology: a case study from the Lévézou massif (French Massif Central, Variscan belt)

C. Lotout [a,b], M. Poujol [a], P. Pitra [a,c], R. Anczkiewicz [d], J. Van Den Driessche [a]

Corresponding author: Caroline Lotout, caroline.lotout@gmail.com

Running title: The fate of Variscan eclogite via petrochronology

[a] Univ Rennes, CNRS, Géosciences Rennes - UMR 6118, F-35000 Rennes, France

[b] Géosciences Le Mans, Le Mans Université, Avenue Olivier Messiaen, 72085 Le Mans CEDEX 9, France

[c] Česká geologická služba, Klárov 3, CZ-118 21 Praha 1, Česká republika

[d] Institute of Geological Sciences, Polish Academy of Sciences, Kraków Research Center, Senacka 1, PL 31-002, Kraków, Poland

Abstract

Linking mineral growth and time is required to unravel the evolution of metamorphic rocks. However, dating early metamorphic stages is a challenge due to subsequent retrograde overprinting. A fresh eclogite and a former eclogite retrogressed under amphibolite facies

from the southern French Massif Central (Lévézou massif, Variscan belt) were investigated with a large panel of geochronometers (U-Pb in zircon, rutile and apatite, Lu-Hf and Sm-Nd in garnet) in a petrological context tightly constrained by petrographic observations, trace element analyses and phase equilibrium modelling. Both samples recorded similar *HP* conditions at 18-23 kbar and 680-800°C, whereas the retrogressed eclogite later equilibrated at 8-9.5 kbar and ca. 600°C. In the retrogressed sample, most of the zircon grains are characterized by negative Eu anomalies and HREE enrichment, and yield an Ordovician U-Pb date of 472.3 ± 1.7 Ma, interpreted as the emplacement age of the mafic protolith. In agreement with other data available for the Variscan belt, and based on zircon trace element record and whole-rock geochemistry, this age is considered to represent the magmatism associated with the extreme thinning of the continental margins during the Ordovician. In the same sample, a few zircon rims show a weaker HREE enrichment and yield a date of 378 ± 5.7 Ma, interpreted as a prograde pre-eclogitic age. Lu-Hf garnet dating from both samples yields identical dates of 357 ± 13 Ma and 358.0 ± 1.5 Ma inferred to approximate the age of the high-pressure metamorphic peak. Fresh and retrogressed samples yield respectively 350.4 ± 7.7 Ma and 352 ± 20 Ma dates for Sm-Nd garnet dating, and 367.8 ± 9.1 Ma and 354.9 ± 9.5 Ma for U-Pb rutile dating. Apatite grains from the retrogressed sample give a mean age of 351.8 ± 2.8 Ma. The similarity between all recorded ages from distinct chronometers and radiometric methods (U-Pb – rutile, apatite; Lu-Hf – garnet; Sm-Nd – garnet) combined with *P–T* estimations from high-pressure metamorphic rocks equilibrated under different conditions testifies to very fast processes that occurred during the Variscan orogeny, highlighting a major decompression of 15-8.5 kbar in less than 7 Myr, and suggesting mean exhumation rates in excess of 6.3 mm/yr.

Keywords: U-Pb zircon, rutile and apatite geochronology, Lu-Hf and Sm-Nd garnet dating, P–T estimates, Petrochronology, High-Pressure metamorphism dating, Exhumation, Variscan Belt, eclogite

INTRODUCTION

High-pressure *(HP*) metamorphism testifies to mountain building processes, including oceanic or continental subduction, as well as crustal thickening. The subsequent exhumation of *HP* rocks is accompanied by retrogression and re-equilibration, driven by a combination of erosion and tectonic processes. Rates and duration of metamorphism – in particular those of *HP* metamorphism that bring invaluable insight into deeply buried terranes – are key parameters to understand the geodynamic evolution of orogens. Numerous studies have attempted to constrain the age of *HP* metamorphism and the subsequent exhumation history by combining several geochronometers, such as U-Pb in zircon, monazite, rutile or titanite, and Lu-Hf and/or Sm-Nd in garnet (*e.g.,* Anczkiewicz *et al*., 2007, 2012; Kylander-Clark *et al*., 2007, 2008; Cheng *et al.,* 2008, 2009, 2012; Warren *et al*., 2012; Colett *et al*., 2018; Lotout *et al*., 2018; Manzotti *et al*., 2018; Butler *et al*., 2018, Cheng *et al*., 2018). The link between these ages and the metamorphic history of the rock, i.e. between time (*t*) and pressure-temperature (*P–T*) evolution, is generally achieved through trace element analysis of the dated minerals (*e.g.,* linking the zircon and garnet growth through their rare-earth-element (REE) patterns, *e.g*., Rubatto, 2002; Whitehouse and Platt, 2003, Taylor *et al*, 2017; Walczak *et al*., 2017; Lotout *et al*., 2018).

In the Variscan belt, the timing of the *HP* metamorphism and the subsequent exhumation of the subducted rocks is controversial. The convergence between two megacontinents, Laurussia to the north and Gondwana to the south, with the contribution of microplates, such as Armorica or Avalonia (*e.g.,* Murphy *et al*., 2009; Kroner & Romer,

2013), induced the closure of oceanic domains, while oceanic rocks were subducted and metamorphosed under *HP* to *UHP* conditions (*e.g.,* Matte, 1986; Lardeaux *et al.,* 2001; Ballèvre *et al*., 2009, 2014). At the scale of the entire Variscan belt, the age of the *HP* metamorphism spreads from the middle to the upper Devonian (see the review of Paquette *et al*., 2017), with the exception of the French Massif Central (FMC). The metamorphic pressure peak in the FMC has long been considered to be late Silurian in age (410-430 Ma), based on only four studies (Pin & Lancelot, 1982; Ducrot *et al*., 1983; Paquette *et al*., 1995; Berger *et al*., 2010; Fig. 1a). Nevertheless, a recent study (Lotout *et al.,* 2018) questioned the validity of these *HP* ages, resulting from outdated methods (*e.g.,* dissolution of fractions of zircon from metamorphic rocks) or over-interpreted data. Based on a multimethod geochronological approach (Lu-Hf and Sm-Nd in garnet; U-Pb in zircon and apatite) this study yielded an age of 376.3 ± 3.3 Ma for the *HP* peak metamorphism in the Najac massif (southern FMC, Fig. 1a). Therefore, in order to decipher the processes involved in the building of the Variscan orogen in the FMC and to document the timing and duration of the *HP* metamorphic event, more petrochronological studies are required.

The Lévézou massif, located only some 70 km to the east of the Najac massif (Fig. 1a), exposes some of the best-preserved eclogites in the FMC and was chosen as the target of a multimethod geochronological study, in order to investigate the timing of *HP* metamorphism in this portion of the European Variscan belt. The strategy is based on a detailed study of two samples from the same *HP* unit: a perfectly preserved eclogite and a former eclogite largely retrogressed under amphibolite-facies conditions. P–T conditions are estimated through a petrographical analysis and numerical modelling of phase equilibria. We then use a large panel of geochronometers (U-Pb on zircon, rutile and apatite, Lu-Hf and Sm-Nd on garnet) combined with trace element analyses in some of the dated minerals (zircon, garnet) on both

samples, to decipher the timing of the *HP* metamorphism and subsequent exhumation of the subducted rocks.

GEOLOGICAL CONTEXT

In the French Massif Central, relics of *HP* rocks are found in the so-called "Leptyno-Amphibolitic Complex" (LAC) (*e.g.,* Forestier, 1971; Santallier *et al.,* 1988; Ledru *et al*., 1989; Bouchardon *et al.*, 1989; Faure *et al*., 2009; Lardeaux, 2014; Fig. 1a). In the Lévézou massif, these *HP* terranes are dominated by mafic and ultramafic rocks with tholeiitic and calc-alkaline affinities (Nicollet, 1978; Piboule, 1979) and contain abundant lenses of eclogite, ± coronitic metagabbro, flaser gabbro, microtroctolite, metadolerite, serpentinite and peridotite. The emplacement of the tholeiitic suite was dated at ca. 485 ± 30 Ma (U/Pb in zircon population from a trondhjemite; Pin, 1979). A gabbro from the calc-alkaline suite was dated at 367 ± 10 Ma with the same method (Pin & Piboule, 1988). No dating of the *HP* metamorphism was ever performed in the Lévézou massif, but it has long been considered as Silurian in age (*e.g.,* Duguet & Faure, 2004; Faure *et al*., 2009; Lardeaux, 2014) based on the similarity with published *HP* ages from other localities of the FMC (Pin & Lancelot, 1982; Ducrot *et al.,* 1983; Paquette *et al.,* 1995; Berger *et al.,* 2010). The validity of these previous studies has been recently questioned (Paquette *et al*., 2017; Lotout *et al*., 2018), and the age of the *HP* metamorphism in the Lévézou massif remains unknown. The upper part of the Lévézou LAC comprises kyanite-garnet bearing micaschists, leucocratic paragneisses and quartzites (Fig.1b). Numerous interpretations have been proposed for the significance of the emplacement of the LAC in the Lévézou massif: (i) Nicollet (1978) suggested that the LAC corresponds to a subducted dislocated ophiolitic sequence; (ii) Piboule (1979) suggested an early intra-continental marginal basin, not fully evolved to an oceanic stage; (iii) Piboule and

Briand (1985) interpreted the LAC as a tholeiitic suite from a shallow crustal origin in a spreading environment; (iv) Pin & Piboule (1988) proposed a collision between two independent magmatic suites to account for the composite character of the LAC; (v) for Briand *et al*. (1988), the magmatic signature of the LAC corresponds to an emplacement in a back-arc basin environment; and (vi) Lardeaux (2014) finally reinterpreted the chemical composition of all the LAC occurrences from the FMC, including the LAC from the Lévézou, as reflecting a hyper-extended continental margin. However, all these authors agree on the fact that the LAC does not correspond to a metamorphosed mature oceanic crust. Despite the controversies on the origin of the LAC and its geodynamic emplacement setting, it is unanimously considered as the tectonic marker of a subduction stage during the Variscan orogeny (*e.g.,* Ledru *et al.,* 1989; Ballèvre *et al.,* 2009; Lardeaux, 2014 and references therein). *P–T* conditions for the *HP* metamorphism in the Lévézou were first estimated at 12.5-20 kbar and 750-840°C (Nicollet & Leyreloup, 1978), then at 16 kbar and 720 ± 30°C (Bouchardon, 1987).

The Lévézou massif (Fig. 1b) is classically subdivided into four superposed units, the Upper Gneiss Unit (UGU), the eclogite-bearing LAC, the Lower Gneiss Unit (LGU), and the Parautochthonous Unit (PAU), from the centre to the outside of the massif. The UGU is composed of paragneisses and felsic orthogneisses, migmatized to various degrees. Mafic enclaves with rare relics of *HP* mineral assemblages, interpreted as xenoliths (Delor *et al*., 1985), are locally found within orthogneisses dated at 468.2 ± 2.7 Ma (Lotout *et al*., 2017). The LGU is composed of amphibolite-facies metasedimentary rocks intruded by several granitic bodies. The Parautochthonous Unit (PAU) is the most external and least metamorphosed unit, and is composed of quartzo-pelitic rocks considered Neoproterozoic to Lower Paleozoic (Nicollet, 1978), micaschists and quartzites with intercalated metarhyolites considered Lower Cambrian, (Collomb, 1964, 1970; Delbos *et al*., 1964). Thrusting of the

UGU and LAC on the LGU, and the underlying PAU, is responsible for an apparent inverted metamorphic zonation (Burg *et a*l., 1989).

ANALYTICAL PROCEDURES

Chemical analyses, mineral composition and *P–T* modelling

The samples were first cleaned from any weathered material, then crushed in a jaw crusher and in an agate mortar to obtain a fine powder. Major and trace elements analyses were performed by Inductively Coupled Plasma Atomic Emission Spectrometry (ICP-AES) and Inductively Coupled Plasma Mass Spectrometry (ICP-MS), respectively, at the Geochemical and Petrographical Research Center (SARM laboratory, CNRS-CRPG) in Nancy, following the procedure described in Carignan *et al*. (2001). FeO (vs. Fe_2O_3) was analysed by wet titration.

Mineral analyses were carried out with a Cameca SX100 electron microprobe (Microsonde Ouest, IFREMER, Plouzané, France) operating in a wavelength-dispersive mode (for the complete analytical procedure, see Pitra *et al*., 2008). Both whole-rock and mineral data were plotted using the software GCDkit (Janoušek *et al*., 2006).

P–T pseudosections have been calculated in the model system Na_2O–CaO–(K_2O)–FeO–MgO–Al_2O_3–SiO_2–H_2O–TiO_2–Fe_2O_3 (NC(K)FMASHTO) using the software Theriak/Domino (de Capitani and Petrakakis, 2010), and the internally consistent thermodynamic data set 5.5 (Holland & Powell, 1998; updated Nov. 2003). Mixing models for solid solutions were taken from Diener & Powell (2012) – amphibole (amph), clinopyroxene (cpx), White *et al*. (2007) – garnet (g), biotite (bi), Holland *et al*. (1998) – chlorite (chl), Holland & Powell (2003) – plagioclase (pl), Holland & Powell (1998) – talc

(ta), epidote (ep), Coggon & Holland (2002) – muscovite (mu) and White *et al*. (2000) – hematite (hem), ilmenite (ilm). Albite (ab), lawsonite (law), quartz (q), rutile (ru) and titanite (sphene, sph) are considered as pure end members. The conversion of the mixing models for Theriak/Domino was obtained from Doug Tinkham (http://dtinkham.net/peq.html).

Other symbols (mole/atomic proportions) used are: X_{Mg} = Mg/(Fe^{2+}+Mg) (garnet, clinopyroxene, amphibole), X_{Ab} = Na/(Ca+Na+K) (plagioclase), X_{Grs} = Ca/(Ca+Mn+Fe^{2+}+Mg), X_{Prp} = Mg/(Ca+Mn+Fe^{2+}+Mg), X_{Alm} = Fe^{2+}/(Ca+Mn+Fe^{2+}+Mg), X_{Sps} = Mn/(Ca+Mn+Fe^{2+}+Mg) (garnet), X_{Jd} = [(2Na)/(Mg+Fe^{2+}+Ca+2Na) x Al^{M1}]/(Fe^{3+}+ Al^{M1}) (clinopyroxene), X_{Ae} = [(2Na)/(Mg+ Fe^{2+}+Ca+2Na) x Fe^{3+}]/(Fe^{3+}+ Al^{M1}) (clinopyroxene); wt% – weight per cent, mol.% – mole per cent, pfu – per formula unit.

The bulk-rock compositions used to calculate the *P–T* diagrams were corrected for the presence of apatite, not considered in the calculations – an amount of CaO equal to 3.33 that of P_2O_5 was allotted for apatite and subtracted from the bulk-rock molar content of CaO (*e.g.,* Pitra & De Waal, 2001; Palin *et al*., 2016). In both samples, H_2O was considered in excess in *P–T* calculations, based on the dehydration character of most metamorphic reactions during prograde metamorphism, leading to H_2O saturation. Furthermore, model predictions, mineral parageneses and mineral chemical compositions are consistent and in good agreement, ascertaining this initial assumption. Manganese has not been taken into account in the modelling because both rocks and their rock-forming minerals (including garnet) are poor in Mn and the mixing models for amphibole and pyroxene used do not include Mn.

LA-ICP-MS dating

A mineral separation procedure has been applied to concentrate zircon, rutile and apatite grains for U-Pb dating using the facilities available at Géosciences Rennes (University

of Rennes 1). The samples were crushed and only the powder fraction with a diameter < 250 µm was kept. Heavy minerals were first concentrated by Wilfley table, then magnetic minerals were removed with an isodynamic Frantz separator. Heavy minerals were afterwards separated with heavy liquids. Zircon, rutile and apatite grains were handpicked under a binocular microscope. The selected minerals were then embedded in epoxy mounts, which were ground and polished on a lap wheel. Zircon and apatite grains were imaged by cathodoluminescence (CL) using a Reliotron CL system equipped with a digital colour camera available at Géosciences Rennes, while rutile grains were imaged by Scanning Electron Microscope using a JEOL JSM 7100 F available at the University Rennes 1 (CMEBA).

U-Pb geochronology of zircon, rutile and apatite grains was conducted by *in-situ* laser ablation inductively coupled plasma mass spectrometry (LA-ICP-MS) at Géosciences Rennes using an ESI NWR193UC Excimer laser coupled to an Agilent quadripole 7700x ICP-MS equipped with a dual pumping system to enhance sensitivity. The instrumental conditions are reported in the supplementary table 1. Further information on the dating protocol is given in in Ballouard *et al*. (2015) for zircon, in Boutin *et al*. (2016) for rutile, and in Pochon *et al*. (2016) for apatite.

Ablation spot diameters of 35 µm and 25 µm (Zrn), 60 µm (Ru) and 45 µm (Ap) with repetition rates of 3 Hz (Zrn) and 5 Hz (Ru, Ap) and a fluence of 8.7 J/cm² were used. Data were corrected for U–Pb and Th–Pb fractionation and for the mass bias by standard bracketing with repeated measurements of the GJ-1 zircon (Jackson *et al*., 2004), R10b for rutile (Zack *et al.,* 2011) and the Madagascar apatite (Cochrane *et al*., 2014). Along with the unknowns, zircon standard Plešovice (Sláma *et al*., 2008), rutile standard R19 (Zack *et al*. 2011), apatite standards McClure (Schoene & Bowring, 2006) and Durango (McDowell *et al*., 2005) were measured to monitor precision and accuracy of the analyses, and produced ages of

336.6 ± 4.1 Ma (Plešovice, N = 6, MSWD = 0.095), 491.8 ± 3.4 Ma (R19, N = 8, MSWD = 0.38), 532 ± 13 Ma (McClure, N = 4, MSWD = 4.4) and 32.5 ± 1.1 Ma (Durango, N = 5, MSWD = 0.34) during the course of the analyses.

Data reduction was carried out with the GLITTER® software package developed by the Macquarie Research Ltd. (Van Achterbergh *et al*., 2001) for zircon, and the data reduction scheme VizualAge_UcomPbine, a set of Iolite procedures that work with Igor Pro (Chew *et al*., 2014) for apatite and rutile. Concordia ages and diagrams were generated using Isoplot 4.15 (Ludwig, 2012). All errors given in supplementary table 2 are listed at one sigma, but where data are combined for Concordia age or weighted mean calculations, the final results are provided with 95 % confidence limits.

Sm-Nd and Lu-Hf dating

Mineral separation was carried out at Géosciences Rennes. Rocks were crushed and**,** from the fraction <500 μm**,** about 70 mg of amphibole for sample LV20B, 70 mg of clinopyroxene from sample LV21 and 200 mg of relatively pure garnet from each sample were handpicked under a binocular microscope. Garnet fractions were subsequently split into three roughly equal aliquots. Additionally, about 100 mg of representative whole rock powder was prepared and used together with garnet and clinopyroxene or amphibole for Lu-Hf and Sm-Nd dating, conducted at the Institute of Geological Sciences, Polish Academy of Sciences, Kraków Research Centre. Leaching, sample dissolution and column chemistry follow procedures outlined in Anczkiewicz & Thirlwall (2003) and Anczkiewicz *et al.* (2004). All measurements were carried out in a static mode using a Neptune multi-collector (MC) ICP-MS applying the protocols similar to those outlined in Thirlwall & Anczkiewicz (2004). Procedure blanks, standards reproducibility, decay constants and reference isotopic ratios

used for the calculations are given in the footnote of table 1. Ages and $^{176}Hf/^{177}Hf$ and $^{143}Nd/^{144}Nd$ initial ratio calculations were conducted by Isoplot 4.15 (Ludwig, 2012). Errors for isotopic ratios are given at the 2 se (standard error) level. Age errors are quoted at 95% confidence level.

Trace element analyses in garnet and zircon

Trace element analyses in garnet (performed in thin section) and zircon (performed in grains mounted in epoxy) were conducted at the Institute of Geological Sciences, Polish Academy of Sciences, Kraków Research Centre, using an Excimer laser (193 nm) RESOlution M50 by Resonetics (now Australian Scientific Instruments) equipped with a S150 dual volume sample cell. Laser ablation was coupled with an ICP-MS XSeriesII by Thermo Fisher. Fluence of about 8 J/cm^2, and 10 Hz repetition rate were applied during the measurements. Analyses of zircon were performed in spot mode with beam size of 29 or 43 μm diameters. The results were normalized to the NIST612 primary standard using the recommended values of Jochum *et al.* (2011). MPI DING glasses served as secondary standards for data quality control. Silica content was used as an internal standard (fixed at 31.5 wt% in zircon). Analyses of garnet profiles were performed in raster mode with a stage speed of 0.250 mm/min and a slit size of 40 μm. More details on analytical conditions are given in Anczkiewicz & Anczkiewicz (2012). Data reduction was carried out using Iolite 3.0 (Paton *et al*., 2010) with the "trace element" data reduction scheme (Woodhead *et al*., 2007).

RESULTS

WHOLE-ROCK GEOCHEMISTRY

Two eclogite samples (LV21 and LV20B) were collected in the LAC of the Lévézou massif, in outcrops close to each other (LV21: 44°12'50"N, 2°40'48"E; LV20B: 44°14'7"N, 2°42'2"E; Fig. 1b). Both samples are calc-alkaline basic rocks (46.53% and 50.58% SiO_2, and 2.61% and 3.05% Na_2O+K_2O, respectively) with high Al_2O_3 and MgO contents (LV20B: 14.53% and 8.54%, respectively; LV21: 18.92% and 11.63%, respectively; supplementary table 3). Al-Fe^T+Ti-Mg and Zr/Ti *vs*. Nb/Y diagrams show that the protoliths of the two eclogitic samples had a basaltic composition (Fig. 2b, d), with a high-Mg tholeiitic chemical character.

REE contents are low in both samples ($\sum$REE = 24.07 and 43.36 for LV21 and LV20B, respectively, Fig. 2a, supplementary table 3). HREE spectra are slightly depleted (Yb/Gd = 0.67-0.72). Light-REE contents are different as the fresh eclogite LV21 is depleted (La/Nd = 0.20), whereas the retrogressed eclogite LV20B shows a slight enrichement (La/Nd = 0.55)

A spider diagram normalized to NMORB immobile elements (Fig. 2c) shows that sample LV21 is systematically depleted in immobile elements. LV20B shows a similar pattern, with the exception of the La, Ce, Pr and Th that are slightly enriched.

Following the classification of Verma *et al*. (2006) for basic rocks based on major element contents, the geochemical contents of the two samples systematically plot within the IAB (Island-Arc Basic rock, see supplementary Fig. 1) domain. Similarly, according to the classification of Hollocher *et al.* (2012), based on the La/Yb – Nb/La ratios, sample LV21 plots within the Oceanic Arc box domain, while LV20B plots within the Continental Arc box domain (supplementary Fig. 2a). The Th *vs*. Nb diagram following Pearce (2008) highlights a crustal contamination for sample LV20B (Th/Yb=0.36 and Nb/Yb=0.49; supplementary

Fig.2b); the Th content was under the detection limit for sample LV21 and was consequently not plotted. Regardless, both samples display an arc-derived chemical character.

PRESSURE AND TEMPERATURE ESTIMATIONS

Fresh eclogite

Petrography

LV21 is a pale isotropic fine-grained eclogite, composed of garnet, omphacite, amphibole, kyanite and rutile. Garnet forms small subhedral grains (40-250 μm) in honeycomb textures along the clinopyroxene and amphibole grain boundaries (Fig. 3a). They are rarely included in clinopyroxene and amphibole. Garnet is inclusion-free, homogeneous, magnesian and chemically not zoned in major elements (X_{Mg} = 0.59-0.66, X_{Prp} = 0.48-0.52, X_{Alm} = 0.27-0.34, X_{Grs} = 0.17-0.22, $X_{Sps} \leq 0.01$; Figs. 3b, c and 4b, e; supplementary table 4). Subhedral tabular crystals of clinopyroxene (80-600 μm) are not zoned in major elements and have the composition of omphacite (X_{Jd} = 0.27-0.31; $X_{Ae} \leq 0.05$; Fig. 4a, supplementary table 4). Few zircon crystals and numerous tiny rutile needles, oriented parallel to the crystal lattice, are commonly concentrated in the core of the omphacite crystals.

Amphibole forms euhedral to subhedral crystals (50-500 μm), which are calcic, non-zoned and chemically homogeneous and span a compositional space between edenite and magnesiohornblende (Si = 6.54-6.72 pfu, Ca = 1.57-1.78 pfu, $(Na+K)_A$ = 0.46-0.57, Ti = 0.05-0.09 pfu , X_{Mg} = 0.92-0.93; Figs 3b, c and 4c, d; supplementary table 4). It locally contains garnet and tiny rutile as inclusions. Rutile occurs as reddish to orange subhedral crystals (50-250 μm) in the matrix, or as needles included in the core of omphacite and

amphibole. Rare elongate kyanite can be observed in the matrix. Sulfides (pyrite, chalcopyrite), zircon and apatite constitute the accessory minerals.

No symplectites developed at the expense of the above-mentioned minerals. Therefore, the sample can be considered as a perfectly preserved, non-retrogressed eclogite. The stable metamorphic assemblage is interpreted as garnet-omphacite-amphibole-kyanite-rutile.

P–T estimates

In order to calculate *P*–T pseudosections, the whole-rock composition was reduced to the NCFMASHTO model system. In particular, K_2O was removed from the bulk, since (i) no K-bearing phase was observed in the thin section, (ii) the amount of K_2O in the bulk rock is very low (0.16 wt%), and (iii) the amphibole model used does not incorporate K.

In the pseudosection (Fig. 5a), the *P–T* stability field corresponding to the inferred eclogite-facies assemblage garnet-omphacite-amphibole-kyanite-rutile is located from ~18 to 24 kbar and 650 to >800°C. It is delimited by the appearance/disappearance lines of chlorite and epidote at low *T*, quartz at low *P,* and amphibole at high *P*. Compositional isopleths and the observed range of X_{Mg} of garnet (0.59-0.66) and amphibole (0.92-0.94) constrain the equilibration conditions at 21-23 kbar and 680-800°C (Fig. 4b). Compositional isopleths have also been calculated for X_{Grs} in garnet, and X_{Jd} and X_{Mg} in omphacite (supplementary Fig. 3). The modelled values are compatible with observations but spread over a very large *P-T* space and are not helpful in better constraining the equilibration *P-T* conditions of the peak assemblage. Mode isopleths calculated for garnet show that garnet can only grow along a prograde *P–T* path (Fig. 5c).

Retrogressed eclogite

Petrography

LV20B is a light greenish fine-grained rock, dominated by garnet and relatively coarse amphibole (up to 2 mm) surrounded by fine-grained symplectites of amphibole, plagioclase and diopside. Also present are minor quartz, epidote, rutile, titanite, biotite, ilmenite, zircon, and apatite. Small subhedral garnet (60-260 μm) has a large core, chemically not zoned in major elements (X_{Mg} = 0.40-0.41, X_{Alm} = 0.45-0.46, X_{Prp} = 0.29-0.32, X_{Grs} = 0.21-0.23, X_{Sps} ~ 0.01) and locally a slightly zoned rim (up to 40 μm thick) marked by a decrease of X_{Mg} (0.40→0.37) and pyrope (0.32→0.26) and a concomitant increase in grossular (0.22→0.28) and spessartine (0.01→0.02; Figs 4b, e, f and 6a, c, d, e, f, supplementary table 4). Garnet locally contains inclusions of epidote, amphibole (50-150 μm) and rarely tiny K-feldspar (< 20 μm). Amphibole spans a compositional space between pargasite, tschermakite and magnesiohornblende (Fig. 4c-d) Based on their textural position, three main types of amphibole can be described. (i) Amphibole 1 forms large anhedral green crystals (0.2-2 mm). They are calcic, magnesian (Ca = 1.80-1.85 pfu; X_{Mg} = 0.73-0.83; Si = 6.53-6.79 pfu; $(Na+K)_A$ = 0.42-0.56 pfu) and have a low Ti content (Ti = 0.04-0.11 pfu). (ii) Small brownish crystals of amphibole 2 (50-250 μm) are commonly closely associated with rutile or surround fine-grained symplectites. They have a calcic and magnesian composition (Ca = 1.84-1.88 pfu; X_{Mg} = 0.69-0.71; $(Na+K)_A$ = 0.47-0.55 pfu, Si = 6.42-6.51 pfu), and show a higher Ti content (Ti = 0.17-0.20 pfu). (iii) Amphibole 3 forms tiny light green crystals (10-50 μm) in symplectites with plagioclase. They are also calcic (Ca = 1.90-1.96 pfu; $(Na+K)_A$ = 0.54-0.60 pfu, Si = 6.35-6.49 pfu), magnesian (X_{Mg} = 0.67-0.76) and display a variable content in

Ti (Ti = 0.05-0.20 pfu). Garnet and amphibole 1 are commonly surrounded by coronae of amphibole 3 + diopside + plagioclase-bearing symplectites.

Ca-clinopyroxene develops in the symplectite, and displays a diopside composition (X_{Ca} = 0.92; X_{Jd} = 0.05; X_{Ae} = 0.03). Epidote occurs as rounded grains disseminated in the matrix, locally as small inclusions (~ 50 μm) in amphibole and garnet. Plagioclase occurs as small crystals in the matrix (100-300 μm), and as tiny lamellae in symplectites (Fig. 6a, d). Despite the different textural position, all crystals have the same composition (X_{Ab} = 0.58-0.69, supplementary table 4). Rutile forms tiny prismatic inclusions (10-75 μm) in amphibole 1 and anhedral grains (100-500 μm) in the matrix (Fig. 6). Brown small biotite crystals (50-200 μm) are localized close to amphibole and rutile (Fig. 6a, d). Quartz grains are observed in the matrix (Fig. 6a, c, d). Based on textural relations, amphibole 1 is interpreted as "primary" and as a part of the original high-pressure assemblage, containing also garnet and rutile. The dominant "secondary" mineral assemblage comprises amphibole 3, plagioclase, diopside, titanite and biotite.

P–T estimates

Calculations were performed in the model system NCKFMASHTO, including K_2O, since biotite is part of the dominant assemblage amphibole-diopside-plagioclase-titanite-epidote-biotite. The corresponding *P–T* stability field is located at <8-12 kbar, <600-700°C (Fig. 7a). It is delimited by the appearance/disappearance of garnet and epidote at high T and plagioclase at high *P*. Compositional isopleths were used to constrain the equilibration conditions of both the dominant (retrograde) and the primary mineral assemblages. The intersection of the isopleths for the Si content of amphibole 1 (Si = 6.5-6.8 pfu) and X_{Mg} of garnet (X_{Mg} = 0.34-0.44) suggests the equilibration of the primary assemblage under eclogite-

facies conditions at 17.5-19 kbar and 680-750°C, in the *P–T* stability field garnet-muscovite-amphibole-clinopyroxene-rutile-quartz ± kyanite (Fig. 7b). Due to the highly retrogressed character of the sample, we cannot ascertain the presence or absence of kyanite to constrain the *P–T* stability field. The intersection of the isopleths for amphibole 3 (Si = 6.35-6.50 pfu) and plagioclase (X_{Ab} = 0.58-0.69) suggests re-equilibration at 600-640°C and 8-9.5 kbar in the stability field plagioclase-biotite-epidote-amphibole-clinopyroxene-quartz-titanite (Fig. 7c).

GARNET TRACE ELEMENT CHEMISTRY AND DATING

Trace element chemistry

Representative trace elements zoning profiles for both samples are shown in Fig. 8. Because of the selected beam size, the Hf contents were below detection limit and could not be measured in thin section. Two representative spectra from each sample were chosen to illustrate the REE variations in garnet. In both samples, the REE contents in whole rock as in garnet, clinopyroxene or amphibole are very low (supplementary table 3).

Zoning profiles in LV21 garnet display various patterns (Fig. 8a, c; supplementary table 5). The first profile displays an "oscillatory zonation". The core of the garnet is composed of a centre characterized by a very low Lu content (down to 0.1 ppm) surrounded by the highest Lu content (~1-1.5 ppm). The surrounding rims show Lu contents decreasing towards the edge (from ~1 to 0.3-0.4 ppm). The second type of profile displays very low Lu content in the inner part of the crystal that tends to increase towards the edge up to 1 ppm. The Sm and Nd contents in both crystal types are low, near or even below the detection limits with the applied analytical conditions, but since the Sm and Nd behaviour is strongly coupled, the zonation trends can be deciphered from Sm alone. The Sm content shows a slight rise

towards the edges (up to 1-2.5 ppm) with the lowest content in the inner part of the crystal (~0.4 ppm).

Zoning profiles in LV20B garnet are similar (Fig. 8b, d; supplementary table 5). The HREE contents are low, Lu contents barely exceeding 2 ppm, but display a typical enriched core (up to 2.5 ppm) – depleted rim (down to 0.5 ppm) zonation. The Sm and Nd values are low, rarely higher than the detection limits. When detected, Sm shows contents ranging from 0.2 to 2 ppm throughout the crystals. Nd contents do not exceed 0.6 ppm in the core of the garnet crystals, but can reach up to ~1.6 ppm in the rims.

Garnet dating

Lu-Hf dating

Lu and Hf contents from sample LV21 were low and practically the same in all analysed garnet fractions, with values in the range of 0.59-0.60 ppm and 0.13-0.14 ppm, respectively (Table 1). These contents are in a good agreement with the LA-ICP-MS measurements performed on garnet in thin section (see Garnet trace element chemistry above). The Hf contents determined by isotope dilution is low, and typical of metamorphic garnet, which suggests that no Hf-rich inclusions disturbed the analyses. The $^{176}Lu/^{177}Hf$ ratios are low (0.629-0.670) but significantly higher than the ones from the WR or the clinopyroxene fractions (0.070 and 0.007 respectively). The isochron yields a date of 357 ± 13 Ma (MSWD = 22; Fig. 9a, Table 1), the low precision being linked to the low $^{176}Lu/^{177}Hf$ ratio and to the excess scatter among the analysed garnet fractions. The accuracy of the results is discussed in the interpretation section below.

The Lu and Hf contents from sample LV20B were also low in all the isotope dilution analyses (Table 1), Lu ranging 0.9-1.3 ppm, and Hf 0.08-0.10 ppm. Similarly, the low Hf values suggest that no Hf-rich inclusion disturbed the analyses. $^{176}Lu/^{177}Hf$ ratios in garnet are higher in this sample (1.74 and 1.76), and significantly different from the $^{176}Lu/^{177}Hf$ ratios of WR and amphibole (0.08 and 0.07 respectively). The significant spread on an isochron allowed to define a date of 357.5 ± 4.0 Ma (MSWD = 16) with an initial $^{176}Hf/^{177}Hf = 0.282862 \pm 56$. The isochron age, calculated without the WR, is similar but more precise at 356.9 ± 1.5 Ma (MSWD = 0.31), and the calculation including the WR and removing the amphibole fractions yields a date of 358.0 ± 1.5 Ma (MSWD = 0.30, initial $^{176}Hf/^{177}Hf = 0.2828450 \pm 76$; Fig. 9b).

Sm-Nd dating

The Sm and Nd contents in LV21 garnet, measured by isotope dilution, are low, ranging 0.63-0.69 ppm and 0.92-1.12 ppm, respectively (Table 1). $^{147}Sm/^{144}Nd$ ratios also display very low values of 0.37-0.42. Analyses of Sm and Nd performed in situ on garnet via LA-ICP-MS directly in thin section were near or below detection limits; consequently, the comparison of Sm/Nd ratios obtained from LA-ICP-MS and dilution, to track possible contamination via unnoticed micro-inclusions, is not appropriate. All the garnet, clinopyroxene and WR fractions yield an isochron date of 350.4 ± 7.7 Ma (MSWD = 1.6) with an initial $^{143}Nd/^{144}Nd = 0.512601 \pm 15$ (Fig. 9c).

The Sm and Nd contents are similarly very low in LV20B garnet, displaying values of 0.60 and 0.64 ppm for Sm and 1.18 and 1.24 ppm for Nd (Table 1). The $^{147}Sm/^{144}Nd$ ratios of the garnet aliquots are low, ranging 0.309-0.311. This ratio is also low for the amphibole and WR fractions, with values of 0.211 and 0.187, respectively. However low, the $^{147}Sm/^{144}Nd$

ratios obtained by isotope dilution are high compared to those obtained by LA-ICP-MS, suggesting the possible contribution of unnoticed microscopic inclusions. The higher contents of Nd compared to Sm (1.18-1.24 and 0.60-0.64, respectively) also suggest the contribution from a Nd-bearing mineral. The two garnet fractions together with the WR and amphibole fractions define a date of 371 ± 12 Ma (MSWD = 2.8). Excluding the WR from the calculation yields a date of 352 ± 20 Ma (MSWD = 0.0058) (Fig. 9d), while excluding the amphibole fraction yields a date of 371 ±12 Ma (MSWD = 0.0095).

ZIRCON DATING AND TRACE ELEMENT CHEMISTRY

Zircon U-Pb dating

Sample LV20B was the only one to provide sufficiently large zircon grains. The crystals are colourless, mostly subhedral to euhedral and range in size from 40 to 350 µm (Fig. 10). A few metamict crystals were avoided during the picking stage. Zircon grains display oscillatory zonation (Fig. 10, zircon grains a and d), patchy zonation (Fig. 10, zircon grains b, e, f) and core and rim textures (Fig. 10c). Where possible, the rims were analysed. Sixty-six analyses were performed out of forty-five zircon grains. Three groups can be distinguished.

(i) A Cambrian group is composed of 11 analyses performed on 9 zircon grains. All analyses are concordant to slightly discordant, and 8 of them allowed us to calculate a Concordia date (as of Ludwig, 1998) of 511.5 ± 4.3 Ma (MSWD = 0.47, Fig. 11a, b). One concordant analysis displays an older date at ca. 570 Ma. Cambrian zircon grains display oscillatory zonation (*e.g.,* Fig. 10, zircon grains a and d) and never exhibit patchy zonation. Their Th/U ratios vary from 0.3 to 0.9, while the U content varies from 28 to 570 ppm (supplementary table 2).

(ii) Ordovician grains define the second group, represented by 47 analyses obtained on 34 zircon grains. The analyses are concordant to discordant. Forty-four analyses provide a lower intercept date of 472.4 ± 1.7 (MSWD = 0.78, Fig. 11a, c, supplementary table 2), while the 32 most concordant analyses yield a Concordia date of 473.4 ± 2 Ma (MSWD = 1.3, Fig. 11c). The three remaining analyses (~450 Ma, supplementary table 2, zr-40, zr-51 and zr-56) are sub-concordant to slightly discordant, and are best explained by variable Pbd loss and common Pb enrichment. The Ordovician zircon dates occurs either in zircon cores (*e.g.,* Fig. 10, zircon c, spot zr-04), or in grains characterized by oscillatory or patchy zoning (*e.g.,* Fig. 10, zircon e, spots zr-40, zr-41, zr-45; zircon f, spots zr-01, zr-02, zr-03). Their Th/U ratios are variable (0.3-1.0) with U contents highly variable between 63 and 799 ppm (supplementary table 2).

(iii) The last group yields Devonian dates, obtained on six analyses from five different zircon grains yielding a lower intercept date of 378.6 ± 5.7 Ma (MSWD = 0.96, Fig. 11a, d). The four concordant analyses yield a Concordia date of 382.3 ± 2.3 Ma (MSWD = 1.4, Fig. 11d, inset). Four analyses were obtained on zircon rims surrounding an Ordovician core (*e.g.,* Fig. 10, zircon a, spot zr-53 and zircon c, spot zr-61), while two analyses correspond to different patchy zoning within a solely Devonian zircon (*e.g.,* Fig. 10, zircon b, spot zr-17 and zr-18). Therefore, the Devonian dates do not correspond to a specific zircon texture. Their Th/U ratios are distributed from 0.4 to 0.6, with U contents ranging from 66 to 220 ppm (supplementary table 2). No correlation can be established between the ages and the U contents or the Th/U ratios.

Finally, in the whole set of analyses, there is no evident pattern linking the texture of the zircon crystals to their apparent ages. Similarly, no obvious link exists between the dates and the U contents (from 28 to 799 ppm) or the Th/U ratios (from 0.3 to 1.0) (supplementary table 2).

Zircon trace element chemistry

The three apparent age groups (Cambrian, Ordovician and Devonian) were also analysed for their trace elements contents, in different textural positions (core, rim, patchy and oscillatory zonation). All REE spectra are variably enriched in HREE (Yb_N/Gd_N = 13.25-78.59, Fig. 12a), and display various Eu anomalies (Eu/Eu* = 0.25-0.71, Fig.12b, supplementary table 6). They are hereafter described according to their measured apparent ages.

Devonian zones were too small to be systematically analysed and consequently only three spots were measured. They systematically display the lowest Ce/Ce* (1.6-6.08) and no or a weak negative Pr/Pr* (0.46-1.06). The Eu anomalies are variable (Eu/Eu* = 0.35-0.71), while HREE are enriched (Yb_N/Gd_N = 44.25-78.59; Fig. 12a). This group nevertheless displays the lowest HREE contents (Gd_N = 8.42-28.66; Lu_N = 1138.98-1892.99). Yttrium contents are also low in this dataset (Y = 211.46-582.05 ppm, Fig. 12b). This group displays the highest U/Yb ratios, ranging 0.72 to 2.78. Ce/Yb and Gd/Yb ratios are of 0.02 and 0.02-0.03, respectively.

Ordovician zones are homogeneous (Fig. 12), all analyses show high Ce anomalies (Ce/Ce* = 14.82-92.35), strongly negative Eu/Eu* (0.25-0.40) and Pr/Pr* (0.10-0.47) and a strong HREE enrichment (Yb_N/Gd_N = 13.25-38.05, av. 27.7). They show high Y (Y = 736.34-3838.82 ppm, Fig. 12) and HREE contents (Gd_N = 46.23-411.44; Lu_N = 2064.17-6764.17) compared to the analyses done in the Devonian zones. This group displays U/Yb ratios ranging 0.41-0.99. Ce/Yb and Gd/Yb ratios are low, from 0.01 to 0.03 and 0.03 to 0.09 (Fig. 12c, d, e, f, supplementary table 6).

Cambrian zones (Fig. 12) display high Ce anomalies (16.62-51.85), low negative Eu anomalies (0.31-0.34), and an enrichment in HREE (Yb_N/Gd_N = 18.83-27.87, av. 21.58). The Pr/Pr* anomaly is highly negative, ranging 0.20-0.28. The Y contents are also high (Y = 1188.14-3422.89 ppm, Fig. 12). This group displays U/Yb ratios from 0.58 to 0.87. Gd/Yb and Ce/Yb ratios are low, ranging 0.04-0.06 and 0.02, respectively (Fig. 12c, d, e, f, supplementary table 6).

Cambrian and Ordovician zones show similar U/Yb, Gd/Yb, Ce/Yb ratios. The few Devonian analyses display similar Gd/Yb and Ce/Yb ratios, but show a higher U/Yb. Despite a small variability, all the analyses fall within the "continental crust zircon" according to provenance diagrams of Grimes *et al*. (2007).

RUTILE GEOCHRONOLOGY

In sample LV21, the dated rutile grains are subhedral, reddish to orange, ranging from 80 to 230 μm in size (Fig. 3a). Seventeen analyses were performed on fourteen rutile crystals. Plotted in a Tera-Wasserburg diagram, all analyses are discordant because of the variable amounts of common Pb and rather low U contents (1.11-2.29 ppm). Nevertheless, all analyses spread on a Discordia and allow for calculation of a fairly well-constrained lower intercept date of 367.8 ± 9.1 Ma (MSWD = 1.5, Fig. 13a, supplementary table 2) with a $^{207}Pb/^{206}Pb$ initial value at 0.891. The weighted average ^{207}Pb-corrected date (calculated at 370 Ma using the Stacey & Kramers (1975) terrestrial Pb evolution model) is equivalent within error at 365.6 ± 8.4 Ma (MSWD = 1.7).

The dated rutile grains from LV20B are reddish to dark, anhedral, with sizes ranging from 80 to 190 μm (Fig. 6a). Eighteen analyses were conducted on 18 rutile grains. All analyses are discordant because of the presence of variable amounts of common Pb. The U

contents in rutile are very low, mostly ranging from 0.9-3.6 ppm except for one analysis with an uranium content of 9.6 ppm. All analyses allow to calculate a lower intercept date of 354.9 ± 9.5 Ma (MSWD = 2.1, Fig. 13b), and a ^{207}Pb-corrected date of 350.6 ± 7.3 Ma (MSWD = 1.6).

APATITE GEOCHRONOLOGY

Apatite grains were found in both samples but were too small in sample LV21 to be analysed. Apatite grains from LV20B are colourless and rounded, ranging in size from 150 to 200 μm. Twenty-three analyses were performed on 23 apatite grains (supplementary table 2). The grains are very homogeneous in cathodoluminescence and characterized by low U (2.0-14.6 ppm) and Pb (0.8-4.2 ppm) contents. All the analysed apatite grains contain some common Pb and therefore plot in a discordant position in a Tera-Wasserburg diagram (Fig. 13c). The resulting Discordia allows to calculate a lower intercept date of 354.6 ± 8.6 Ma (MSWD = 0.44) with a ^{207}Pb/^{206}Pb initial value of 0.901. The weighted average ^{207}Pb-corrected date (calculated at 350 Ma using the Stacey and Kramers (1975) terrestrial Pb evolution model) is equivalent within error at 351.8 ± 2.8 Ma (MSWD = 0.98, Fig. 13d).

INTERPRETATION AND DISCUSSION

From dates to ages

Zircon

Th/U ratios range from 0.33 to 1.01, a range that is much higher than the usual values expected for metamorphic zircon (<0.1, Rubatto, 2002). Nevertheless, the sample does not contain Th-rich minerals, such as, monazite or allanite, which could explain these higher Th/U ratios as suggested by Harley *et al*. (2007).

The Cambrian and Ordovician dates display true "magmatic-like" spectra (marked negative Eu anomaly and enrichment in HREE, *e.g.,* Rubatto, 2002). The concordant date of 473.4 ± 2 Ma is well recorded by the majority of zircon grains from this sample and is equivalent to the emplacement age of the neighbouring orthogneisses (ca. 470 Ma, Lotout *et al*., 2017). Accordingly, it is proposed that this date of 473.4 ± 2 Ma corresponds to the emplacement and crystallization of the protolith of the metabasic rocks. The cluster of 9 zircon grains that recorded an older Cambrian date (grains free of any rims or cores) could correspond to xenocrysts (*i.e*., contamination) coming from the intruded rocks (not dated but considered Cambrian-Ordovician in the literature, *e.g.,*, quartzo-pelitic rocks from the PAU, considered Neoproterozoic to Lower Paleozoic, Nicollet (1978); the metarhyolites from the PAU considered Lower Cambrian, Collomb (1964)). Moreover, magma-crust interaction is highlighted in sample LV20B (see Whole rock geochemistry section and supplementary Fig. 2b), and therefore support the crustal contamination origin for the Cambrian zircon.

The 378.6 ± 5.7 Ma date is poorly recorded and obtained in zircon zones displaying less-enriched HREE patterns, lower Eu anomalies (0.4-0.8), lower Th/U ratios (0.34-0.59), and lower Y contents (~200-600 ppm). This chemistry, although different from that of magmatic zircon, is not characteristic of eclogitic zircon, which is expected to display no HREE enrichment, no Eu anomaly, and Th/U < 0.1 (Rubatto, 2002). This spectrum is likely to correspond to zircon growth or recrystallization during a metamorphic reaction on the prograde path, prior to the eclogite facies.

Garnet

The first profile from sample LV21 (Fig. 8a) shows, despite the low Lu contents, a depleted inner core surrounded by Lu highs and a rimward depletion. The second profile from the same sample does not show the Lu highs in the garnet core. Instead, it shows that the edges are apparently slightly enriched in Lu. All Lu profiles in garnet LV20B show a systematic classic Rayleigh fractionation (enriched core evolving to depleted rim).

Garnet grains, in the two samples, belong to the *HP* assemblage (peak estimated at 18-23 kbar, 680-800°C). The Lu-Hf results in both samples yield comparable dates around ~358 Ma. Three generations of amphibole are described in the retrogressed sample and despite a careful attention during the hand-picking procedure to select only the large greenish amphibole 1, possible contamination with amphibole crystals of the second or third generation cannot be excluded. Consequently, the use of garnet and WR aliquots to calculate an isochron appears more appropriate, and the corresponding date of garnet from LV20B is therefore 358.0 ± 1.5 Ma (MSWD = 0.30). Despite the low precision in LV21 (357 ± 13 Ma, MSWD = 22), Lu-Hf dates obtained on garnet from both the retrogressed and the fresh eclogitic samples are equivalent within error, suggesting that these dates are accurate and geologically meaningful. The Lu zoning in garnet grains from LV20B shows a typical core-enriched and rim-depleted pattern, which is consistent with a growth zoning. The age obtained from LV20B is therefore mostly controlled by the core and approximates the early growth of the garnet crystals. Garnet from the sample LV21 displays the opposite trend, with Lu-enriched rims, suggesting that the Lu-Hf garnet date is the best estimate for garnet crystallization at peak pressure. Even considering the highest *T* estimation modelled for the rocks (800°C), the *T* necessary for an effective diffusion of Lu and Hf is higher (*e.g.,* Anczkiewicz et al., 2007,

Smit et al., 2013), and consequently, this did not affect the calculated dates. The similarity between the two dates, despite the opposite Lu zoning trend (Lu-enriched cores vs. Lu-enriched rims), is then best explained by incipient crystallization and fast further growth of garnet at 358.0 ± 1.5 Ma.

In both samples, Sm and Nd show very low contents which, when successfully analysed, lead to incomplete profiles that are difficult to interpret. Nevertheless, in all profiles, Nd and Sm contents appear to be slightly higher in the rims, a feature typical of incompatible element behaviour. LV21 yields a Sm-Nd date of 350.4 ± 7.7 Ma, equivalent, within error, to the Lu-Hf date obtained in the same sample. The temperatures reached by the rocks are largely above the Sm-Nd closure temperature commonly accepted for garnet (ca. 650-700°C for the concerned grain size; *e.g.,* Tirone *et al*., 2005; Smit *et al.*, 2013), which suggests that the Sm-Nd date of 350.4 ±7.7 Ma corresponds to cooling during exhumation.

The LV20B Sm-Nd data, when all fractions are used in the calculation, yield a date of 371 ± 12 Ma, significantly older than the Lu-Hf date of 357 ± 4 Ma recorded on the same aliquots. Excluding the amphibole fraction from the calculation yields similar results, while excluding WR yields a poorly constrained date of 352 ± 20 Ma, similar to the one recorded in the fresh sample LV21. The low Sm/Nd ratios, the stability of epidote in the sample, and Nd contents higher than the Sm contents suggest a possible Nd-rich inclusion contamination in the dated garnet aliquots. This issue seems corroborated by the different ages calculated using (or not) the WR or amphibole aliquots. Therefore, the Sm-Nd date obtained from LV20B has to be disregarded to decipher the *P–T–t* evolution of the sample, and to discuss the large-scale evolution of the eclogitic terranes of the Lévézou massif.

Rutile

The recorded date of 367.8 ± 9.1 Ma (MSWD = 1.5, N = 16) in the fresh sample is analytically good (good spread, valid $^{207}Pb/^{206}Pb$ initial value) and is equivalent within error to the date recorded in garnet from the same sample (Lu-Hf: 357 ± 13 Ma). Similarly, rutile analyses from the retrogressed sample provide a lower intercept date of 354.9 ± 9.5 Ma (MSWD = 2.1), which is equivalent within error to the recorded Lu-Hf garnet date (358.0 ± 1.5) and to the rutile date from the fresh sample. Petrographically, rutile from the retrogressed sample is not in equilibrium with the dominant (retrograde) assemblage and is interpreted as a relic of the *HP* paragenesis. Nevertheless, the closure temperature of the U-Pb system in rutile is strongly controlled by the grain size (~ 600-650°C in crystals with size ranging from ~ 100 to ~ 200 µm; *e.g.,* Cherniak, 2000; Vry & Baker, 2006) and is significantly lower than the maximum *T* attained during the metamorphic peak (680-800°C). Indeed, rutile is commonly used as a thermochronometer to constrain the cooling history of metamorphic terranes (*e.g.,* Mezger *et al*., 1989, 1991; Zack *et al*., 2004, 2011; Kylander-Clark *et al.,* 2008; Kooijman *et al*., 2010). Consequently, we interpret the rutile U-Pb dates as corresponding to cooling during exhumation. The similarity of these dates with the Lu-Hf ages (interpreted to date both the incipient crystallization and further growth of garnet) suggests that the entire process of subduction (and associated prograde garnet growth) and subsequent exhumation and cooling must have been quick.

Apatite

Apatite grains are dispersed in the matrix and cannot be attributed to any part of the metamorphic history based on petrographic observations. They could have crystallized during the magmatic stage and been re-equilibrated during the metamorphic history of the rock, or crystallized anywhere along the *P–T* path. U-Pb on apatite is commonly considered as a

medium temperature chronometer since its Pb closure temperatures (T_c) are generally comprised between 375 and 500°C (*e.g.,* Cherniak *et al*., 1991; Chamberlain & Bowring 2001; Harrisson *et al*., 2002; Schoene & Bowring 2007; Cochrane *et al*., 2014). Based on the results of this study, we calculated the apatite T_c of these grains using the equation of Dodson (1973) and data from Cherniak *et al*. (1991). We used a radius of 75 to 100 μm, assuming a spherical form of the dated apatite crystals. Various cooling rates ranging 200°C/Myr to 5°C/Myr were used based on the results obtained in this study (Lu-Hf age of 357.5 ± 4 Ma, apatite age of 351.8 ± 2.8 Ma, modelling *T* estimates of 680-800°C during the metamorphic peak to the 620-600°C attained during the retrogression). The highest cooling rate of 200°C/Myr corresponds thus to a minimal Δt of 1 Myr and a maximal ΔT of 200°C, whereas the lowest cooling rate of 5°C/Myr corresponds to a maximal Δt of 12 Myr and a minimal ΔT of 60°C. The recalculated T_c of apatite then ranges from 510 to 590°C, consistent with the higher range of the published data. In case of very fast processes, higher T_c values are indeed expected, and already described in a study of dyke emplacement (Pochon *et al*., 2016; maximum T_c for apatite of 770-870°C). The temperature reached by the rocks is high (680-800°C) and consequently we consider that the date of 354.6 ± 8.6 Ma (mean age at 351.8 ± 2.8 Ma) corresponds to the cooling during the exhumation of the terranes.

Eclogite protoliths: origin and emplacement setting

Both the basic character of the chemical compositions and the major elements discrimination diagrams (Fig. 2) suggest a basaltic or gabbroic protolith for both samples. Furthermore, the honeycomb texture observed in the fresh eclogite has already been interpreted as pseudomorphing a gabbroic texture (Lasnier, 1970, 1977). Finally, the presence

of tiny rutile needles in the core of omphacite crystals suggests that they are the result of the destabilisation of a magmatic Ti-rich clinopyroxene.

The zircon U-Pb age of 473.4 ± 2 Ma obtained in this study, similar to the age of the emplacement of the adjacent granite dated at 468.2 ± 2.7 (Lotout *et al*., 2017), provides new evidence of the bimodal character of this massive magmatic event recorded during the Ordovician (*e.g.,* Iberian Massif – *e.g.,* Sánchez-García *et al*., 2003, 2008; Villaseca *et al*., 2015; Del Grecco *et al*., 2016; Gutiérrez-Alonso *et al*., 2016; García-Arias *et al*., 2018; Armorican Massif – *e.g.,*, Ballèvre *et al*., 2012, Paquette *et al*., 2017; French Massif Central – *e.g.,*, Pitra *et al*., 2012; Chelle-Michou *et al*., 2017; Lotout *et al*., 2017; Sardinia – *e.g.,*, Helbing & Tieppolo, 2005; Oggiano *et al*., 2010; Caggero *et al*., 2012; Bohemian Massif – *e.g.,* Košler *et al*., 2004; Linnemann *et al*., 2008), related to the extreme stretching of the lithosphere (*e.g.,* Bard *et al*., 1980; Matte & Burg, 1981; Matte, 1986; Pin, 1990; Ribeiro *et al*., 2007; Martínez Catalán *et al*., 2009; Lardeaux, 2014; Schulmann *et al*., 2014).

Tectonic fingerprinting based on major and trace elements discrimination diagrams is commonly used since the early 70s (*e.g.,* Pearce & Cann, 1971; Wood, 1980). However, the use of major-element-based discrimination diagrams to characterize the tectonic setting of the protolith of metamorphosed rock is debatable due to major element mobility (*e.g.,* Agrawal *et al*., 2008). In this study, both major and trace element-based diagrams (geotectonic diagrams following Verma *et al.,* 2006, supplementary Fig.1, and Hollocher *et al.,* 2012, supplementary Fig. 2a; REE normalized to chondrite spectra, trace elements normalized to NMORB spider diagrams, Fig 2a, c) highlight a depleted MORB signature and an island-arc tectonic setting. Following the Pearce (2008) Th/Yb *vs*. Nb/Yb diagram (supplementary Fig. 2b), the LV20B chemical composition highlights interaction between mafic magma and crust.

The zircon trace element content is widely used to interpret zircon ages in metamorphic rocks (*e.g.,* co-eval growth of a HREE-bearing mineral as garnet, Rubatto, 2002; Whitehouse & Platt, 2003), to decipher magmatic processes (magma-chamber evolution – *e.g.,*, Claiborne *et al*., 2006) or to identify the provenance of detrital grains (*e.g.,* Belousova *et al*., 2002; Grimes *et al.*, 2007, 2015). In the U/Yb vs Y or Hf diagrams (Fig. 12), the analysed zircon crystals systematically fall within the "continental zircon" array, according to the provenance diagrams of Grimes *et al.* (2007), which could suggest a contamination of the mafic magma by surrounding crustal material.

By combining the results of whole-rock based major and trace element geotectonic diagrams with the zircon trace element provenance diagrams, all results suggest a crustal contamination (Fig. 2) and are in agreement with previous studies that suggested emplacement in a thinned continental crust in a spreading environment (*e.g.,* Briand & Piboule, 1985; Briand *et al.*, 1988; Bouchardon *et al*., 1989).

Validity of the *P–T* estimates

The *P–T* estimations obtained from numerical modelling and mineral chemical compositions in both the fresh and the retrogressed sample highlight a similar *HP* metamorphic peak at 18-23 kbar and 680-800°C (Figs 5, 7, 14). The *P* estimates from both samples are slightly higher than the previous estimations of Nicollet & Leyreloup (1978; 12.5-20 kbar and 750-840°C) and Bouchardon (1987; 16 kbar and 720 ± 30°C), whereas the *T* estimates are equivalent and in good accordance with these two previous studies.

Timing and duration of metamorphism: stages and rates

Geothermal gradient at the HP peak

Assuming lithostatic *P* and a maximum *P* of 21-23 kbar, there are three end-member possibilities to calculate the geothermal gradient. (i) First, it can be assumed that the increase in *P* is only the result of a crustal thickening. In this case, assuming a density (*d*) of 2.7-2.9 g/cm^3, rocks would have reached a depth of 72-85 km. (ii) However, in a subduction-zone setting, the contribution of both the crust and the mantle in the overlying rock column should be taken into account. A second way to calculate the geothermal gradient would then be to use a continental crust of 30 km (d = 2.7 g/cm^3), which corresponds to 8.1 kbar. The remaining 12.9-14.9 kbar then relate to the *P* applied by the mantle-rock column (d = 3.3 g/cm^3), which corresponds to a depth of 39-45 km. In this scenario, rocks would have reached a depth of 69-75 km. (iii) Finally, in a context of an oceanic subduction below an extremely attenuated continental margin, the thickness of the continental crust can be neglected (*e.g.*,, subduction below an arc), so that rocks reached a depth of 63-69 km.

Consequently, considering a subduction-zone setting, the maximum depth reached by the rocks ranges 63-75 km. The *T* estimates vary from 680 to 800°C at the metamorphic peak, and therefore, the geothermal gradient ranges from 9.1°C/km to 12.7°C/km. *P*–T data from eclogites of the nearby Najac massif (Lotout *et al*., 2018) yield a similar gradient of ca. 8.5-12.4°C/km. These geothermal gradients are consistent with a Palaeozoic subduction zone (see the review of Brown, 2014).

Timing of the metamorphic events: eclogitic peak and retrogression

Garnet Lu-Hf and Sm-Nd, rutile U-Pb and apatite U-Pb dating yield similar ages within error (Fig. 14). Considering the temperature conditions at the peak metamorphic *P*, the grain size and the garnet zoning (Lu-enriched core), we infer that the Lu-Hf age obtained from LV20B at 358.0 ± 1.5 Ma is biased toward the core and reflects prograde garnet growth.

The comparable age of the LV21 garnet, which displays a distinct zoning with Lu-enriched rims, suggests fast garnet growth. Consequently, the Lu-Hf age at 358.0 ± 1.5 Ma is likely to well approximate the *HP* metamorphic peak at 18-23 kbar and 680-800°C. The results of garnet Sm-Nd (350.4 ± 7.7 Ma) and rutile U-Pb (354.9 ± 9.5 Ma), whose T_c are ca. 600-700°C, are then considered to date the cooling during the exhumation stage to 8-9.5 kbar and 600-620°C, conditions of the development of the dominant retrograde assemblage in LV20B. The consistency and similarity of all different ages and chronometers support this interpretation.

Rates of exhumation

Following the *P-T* estimates and radiometric results from this study, the drop in *P* from 18-23 kbar to 8-9.5 kbar started at ca. 358.0 ± 1.5 Ma (Lu-Hf garnet age) and was achieved before 351.8 ± 2.8 Ma, based on the T_c of apatite (510-590°C) being lower than the *T* estimate at this *P* (600-620°C). The drop in *P* is then between 15 and 8.5 kbar, with an average of 11.7 kbar. Assuming lithostatic *P*, this exhumation consequently started at mantle depths and the subducted material underwent an exhumation of 33-45 km, with an average of 39 km. Exhumation started at 358.0 ± 1.5 Ma and was achieved before 351.8 ± 2.8 Ma, lasting an average of 6.2 Myr; by taking maximum errors into account, the slowest and fastest exhumation processes lasted 10.5 Myr and 1.9 Myr, respectively. Consequently, exhumation rates for a vertical exhumation range from a minimum of 3.1 up to 23.7 mm/yr, with a median value of 6.3 mm/yr.

These rates are markedly faster than the mean erosion rates in mountain belts, estimated between 0.1 and 3 mm/yr for a long-lived thickened crust (*e.g.,* Leeder, 1991; Avouac & Burov, 1996). Consequently, the calculated rates from this study suggest that exhumation was mostly driven by tectonic processes.

Tectonic implications

The Variscan orogeny in the French Massif Central

Our results question the previous models proposed for the tectonic evolution of the Lévézou massif (*e.g.,* Burg & Teyssier, 1983; Burg *et al*., 1989; Duguet & Faure, 2004).

According to Duguet & Faure (2004), a top-to-the-South-West major nappe stacking occurred at around 380 Ma. It involved the emplacement of the LAC and resulted in a thickened continental crust. It was followed by a late top-to-the-North-West transpressive event at 360 Ma. This implies that the eclogite-facies metamorphism in the Lévézou massif developed prior to 380 Ma, as previously suggested (Pin & Lancelot, 1982; Burg *et al*., 1989; Duguet & Faure, 2004). Here we show that the eclogitic terranes were buried to depths of 63-75 km, then exhumed to a depth of 30 km at ca. 352 Ma. Considering (i) the inferred geothermal gradients (9.1-12.7°C/km) and the mafic character of the unit, and (ii) the timing of burial and exhumation, the burial of the eclogitic terranes in this area developed within a subduction zone, which is consistent with previous interpretations (*e.g.,* Burg *et al*., 1989). We therefore conclude that crustal thrusting in the Lévézou massif did not occur prior to 352 Ma.

The age of the *HP* event in the Lévézou massif is significantly younger than the recent *HP* age described in the neighbouring Najac massif, where the *HP* peak is estimated at 376 ± 3.3 Ma (Lotout *et al*., 2018; Fig. 15). This diachronism can be explained by either (i) the dating of rocks in distinct initial tectonic settings (terranes distal *vs.* proximal to the continental margin), (ii) closure of different oceanic domains, (iii) an oblique convergence inducing a diachronous closure of the ocean, or (iv) an active subduction zone where slices of buried crust are episodically exhumed.

(i) The first hypothesis implies that the older *HP* ages (Najac) reflect the subduction of oceanic terranes, while the younger recorded dates correspond to the subduction of more continental terranes. The Lévézou massif displays depleted tholeiitic MORB chemical compositions (Briand *et al*., 1988, this study) and has been described as a dismembered ophiolitic sequence (Nicollet, 1978). Moreover, if this scenario is correct, one would expect distinct prograde gradients between these two units, corresponding to the subduction of oceanic and continental material, which is not the case. Consequently, this hypothesis seems unlikely. (ii) Different oceanic domains would imply that different continental blocs are involved in the FMC architecture, i.e. that each *HP* unit corresponds to a specific subduction zone. Considering geodynamic reconstructions and paleomagnetic constraints (*e.g.,* Edel *et al*., 2018 and references therein), such a hypothesis suggesting numerous subduction zones within the FMC is highly unlikely. (iii) A diachronous closure of an oceanic domain, *i.e*., an oblique convergence, could be plausible at the scale of the FMC, but this would imply the occurrence of major transfer faults, not yet identified. (iv) Finally, the episodic exhumation of *HP* terranes in an active subduction setting could be a likely explanation for the record of different *HP* ages. Indeed, the similarity of the geothermal gradients inferred in the Lévézou massif (9.1-12.7°C/km) and the nearby Najac massif (8.5-12.4°C/km) strongly suggests a common tectonic context and favours the hypothesis of an active subduction setting.

In the eastern part of the French Massif Central a protracted magmatic activity is well described, with ages younging from the N to S, from ca. 340 to 300 Ma. The chemical composition of the rocks suggests a coeval mantle- and crust-derived magmatism (Couzinié *et al*., 2014, Laurent *et al*., 2017), interpreted as resulting from either a slab retreat or a retro-delamination of the lithospheric mantle, during the collisional stage. The UGU in this eastern part of the FMC has experienced amphibolite- to granulite-facies metamorphism from 360 to 340 Ma, interpreted as resulting from the collisional stage (Chelle-Michou *et al*., 2017). This

new age of 360 Ma for the *HP* peak metamorphism in the Lévézou massif highlights differences in the timing of the metamorphic stages and/or in the units correlation within the FMC. Consequently, to link the western and eastern part of the FMC and discuss large-scale building processes, geochronological constraints on the timing and duration of the *HP* metamorphism in the eastern part of the FMC are of critical importance.

Exhumation process of HP rocks in the French Massif Central

How *HP* rocks return to the surface has been poorly addressed in the Variscan French Massif Central, as well as in the Variscan belt as a whole. The large time lapse between the presumed age of the *HP* metamorphism and the subsequent Barrovian metamorphism related to crustal thickening led most proposed tectonic models to implicitly invoke long-term erosion as the main process to achieve exhumation of *HP* rocks (*e.g.,* Gardien *et al*., 1990; Lardeaux *et al*., 2001). Our data, however, show that the age of the *HP* metamorphism in the Lévézou Massif is much younger than previously thought and that most exhumation occurred very fast after the pressure peak. The short time lapse between the deep burial and subsequent exhumation invalidates erosion as the dominant process for exhumation because it implies too fast, unrealistic mean erosion rates (in excess of 5 mm/yr). Numerous tectonic models have been proposed in modern orogens to explain such features. It is beyond the scope of the present paper to discuss the different aspects of these models (see *e.g.,* Brun & Faccenna, 2008). However, we would like to highlight that the Variscan belt has been long described as a collision belt of the Himalaya-Tibet type, especially for the FMC (Matte, 1986). Tectonics of the Variscan belt of Europe has been recently better interpreted as the result of amalgamation of small continental blocks and insular arcs that resulted from the extreme stretching and thinning of the initial Gondwana margin during the Late Paleozoic, before the final collision with Laurasia (*e.g.,* Lardeaux *et al*., 2014). In this sense, early Variscan tectonics, including the *HP* metamorphic event and subsequent rock exhumation, should rather be compared to the

Aegean tectonics during the Cenozoic (*e.g.,* Brun & Faccenna, 2008) than to the India-Asia collision (*e.g.,* Mattauer, 1986). According to Lotout (2017), most of the Lévézou massif, including the felsic orthogneiss-bearing core, has been subducted up to 45-50 km 360 Ma ago. The granitic orthogneiss protolith has been dated at 470 Ma (Lotout *et al*., 2017) and belongs to the widespread magmatism that developed during the Ordovician extension. This was at the origin of the breaking up of the Gondwana margin and the opening of several, more or less restricted oceanic domains, separated by small continental blocks (*e.g.,* Lardeaux *et al*., 2014). According to Brun & Faccenna (2008), such subduction of small continental blocks may trigger slab rollback that creates the space required for exhumation of the previously deeply buried rocks. Increasing buoyancy during the subduction eventually results in the detachment of the crust from the plunging slab and in the subsequent fast exhumation of *HP* rocks at a rate that depends on that of the trench retreat.

We suggest that both the *HP* metamorphism and the exhumation of the *HP* rocks in the Lévézou were controlled by subduction dynamics from 360 Ma to 350 Ma, before the later collisional stage responsible for the final structural pattern in a complex folded nappe of the Lévézou massif as a whole (*e.g.,* Burg *et al.*, 1989; Duguet & Faure, 2004) (Fig. 1b).

CONCLUSIONS

This study combines for the first time the estimates of *P-T* conditions of two samples from the same *HP* unit that preserved distinct metamorphic stages with the dating of available geochronometers (garnet, rutile, apatite, zircon). It demonstrates a crystallization age of 473.4 ± 2 Ma for the mafic eclogite protolith. Based on a petrochronological multi-method study and thermodynamic modelling on an eclogite and a former eclogite retrogressed under amphibolite facies, we show that the Lévézou eclogites reached 680-800°C at 18-23 kbar. The

age of the *HP* peak is estimated at ~ 359 Ma, while subsequent exhumation to 8-9.5 kbar and ca. 600°C is completed by ~ 352 Ma, suggesting fast exhumation rates in excess of 6.3 mm/yr. This study provides the first dating of the *HP* event in the Lévézou massif. The similarity between all recorded ages from distinct chronometers (U-Pb – rutile, apatite; Lu-Hf – garnet; Sm-Nd – garnet) combined with tightly constrained *P–T* estimations from *HP* metamorphic rocks equilibrated under different conditions in the Lévézou massif exemplify a short time lapse between the *P-T* peak, exhumation and cooling. A tectonic environment facilitating fast exhumation of deeply buried terranes, as slab rollback or upper plate retreat, is then likely to have occurred during the Variscan orogeny. Finally, the use of multiple petrochronometers in samples belonging to distinct metamorphic stages is an asset to constraining and understanding their geodynamic evolution.

Acknowledgements

We sincerely thank X. Le Coz for thin section preparation, Y. Lepagnot for sample crushing, M. Smędra and D. Sala for the help with the Sm-Nd and Lu-Hf chemical procedure, and J. Langlade for the help with microprobe analysis. M. Ballèvre is thanked for stimulating discussions about the Variscan geodynamics, and providing the file for Figure 15. SEM images were performed at CMEBA facility (ScanMAT, UMS 2001 CNRS − University of Rennes 1) which received a financial support from the European Union (CPER-FEDER 2007−2014, Présage n° 39126 and Présage n° 37339). The U-Th/Pb data were obtained with the analytical equipment from the GeOHeLiS Platform (University of Rennes 1 This work was partly financed by an internal grant from the OSUR (Université Rennes 1), an INSU-CNRS (TelluS 2017) project, and internal CGS grant 310400, accorded to P. Pitra. This study is a part of the PhD thesis of C. Lotout, funded by the French Ministry of higher education and research. We sincerely thank Marián Janák, Arne Wilner and Besim Dragovic for their constructive

reviews as well as the editorial handling of Reto Gieré and Marjorie Wilson; their input improved the clarity and the overall appeal of the manuscript.

References

Agrawal, S., Guevara, M., & Verma, S. P. (2008). Tectonic discrimination of basic and ultrabasic volcanic rocks through log-transformed ratios of immobile trace elements. *International Geology Review* **50**, 1057-1079.

Anczkiewicz, A.A. & Anczkiewicz, R. (2012). U–Pb zircon geochronology and anomalous Sr-Nd-Hf isotope systematics of late orogenic andesites: Pieniny Klippen Belt, Western Carpathians, South Poland. *Chemical Geology* **427**, 1-6.

Anczkiewicz, R., Platt, J.P., Thirlwall, M.F. & Wakabayashi, J. (2004). Franciscan subduction off to a slow start: evidence from high-precision Lu–Hf garnet ages on high grade-blocks. *Earth and Planetary Science Letters* **225**, 147-161.

Anczkiewicz, R., Szczepański, J., Mazur, S., Storey, C., Crowley, Q., Villa, I.M., Thirlwall, M.F. & Jeffries, T.E. (2007). Lu–Hf geochronology and trace element distribution in garnet: implications for uplift and exhumation of ultra-high pressure granulites in the Sudetes, SW Poland. *Lithos* **95**, 363-380.

Anczkiewicz, R. & Thirlwall, M.F. (2003). Improving precision of Sm-Nd garnet dating by H2SO4 leaching: a simple solution to the phosphate inclusion problem. *Geological Society, London, Special Publications* **220**, 83-91.

Anczkiewicz, R., Thirlwall, M., Alard, O., Rogers, N.W. & Clark, C. (2012). Diffusional homogenization of light REE in garnet from the Day Nui Con Voi Massif in N-Vietnam:

Implications for Sm-Nd geochronology and timing of metamorphism in the Red River shear zone. *Chemical Geology* **318**, 16-30.

Avouac, J. P., & Burov, E. B. (1996). Erosion as a driving mechanism of intracontinental mountain growth. *Journal of Geophysical Research: Solid Earth*, **101**, 17747-17769.

Ballèvre, M., Bosse, V., Ducassou, C. & Pitra, P. (2009). Palaeozoic history of the Armorican Massif: models for the tectonic evolution of the suture zones. *Comptes Rendus Geosciences* **341**, 174–201

Ballèvre, M., Catalán, J.R.M., López-Carmona, A., Pitra, P., Abati, J., Díez Fernández, R., Ducassou, C., Arenas, R., Bosse, V., Castiñeiras, P., Fernández-Suárez, J., Gómez Barreiro, J., Paquette, J.L., Peucat, J.J., Poujol, M., Ruffet, G. & Sánchez Martínez, S. (2014). Correlation of the nappe stack in the Ibero-Armorican arc across the Bay of Biscay: a joint French-Spanish project. In: Schulmann, K., Catalán, J.R.M., Lardeaux, J.M., Janoušek, V., Oggiano, G., (eds) *The Variscan orogeny: extent, timescale and the formation of the European Crust*. Geological Society London **405**, 77-113.

Ballèvre, M., Fourcade, S., Capdevila, R., Peucat, J.J., Cocherie, A. & Fanning, C.M. (2012). Geochronology and geochemistry of Ordovician felsic volcanism in the Southern Armorican Massif (Variscan belt, France): Implications for the breakup of Gondwana. *Gondwana Research* **21**, 1019-1036.

Ballouard, C., Boulvais, P., Poujol, M., Gapais, D., Yamato, P., Tartèse, R. & Cuney, M. (2015). Tectonic record, magmatic history and hydrothermal alteration in the Hercynian Guérande leucogranite, Armorican Massif, France. *Lithos* **220-223**, 1-22.

Bard, J. P., Burg, J. P., Matte, P. & Ribeiro, A. (1980). La chaine hercynienne d'Europe occidentale en termes de tectonique des plaques. *Géologie de l'Europe* **108**, 233-46.

Bas, M.L., Maitre, R.L., Streckeisen, A., Zanettin, B., (1986). A chemical classification of volcanic rocks based on the total alkali-silica diagram. *Journal of petrology* **27**, 745-750.

Berger, J., Féménias, O., Ohnenstetter, D., Bruguier, O., Plissart, G., Mercier, J.C. & Demaiffe, D. (2010). New occurrence of UHP eclogites in Limousin (French Massif Central): Age, tectonic setting and fluid–rock interactions. *Lithos* **118**, 365-382.

Belousova, E., Griffin, W. L., O'Reilly, S. Y., & Fisher, N. L. (2002). Igneous zircon: trace element composition as an indicator of source rock type. *Contributions to mineralogy and petrology* **143**, 602-622.

Bouchardon, J.L., 1987. Evaluation des conditions de pression-temperature du "top" mttamorphique des eclogites du Levezou (Rouergue Massif Central Français). *CR. Acad. Sci. Paris* **305**, 271-275.

Bouchardon, J.L., Santallier, D., Briand, B., Ménot, R.P. & Piboule, M. (1989). Eclogites in the French Palaeozoic Orogen: geodynamic significance. *Tectonophysics* **169**, 317-332.

Boutin, A., de Saint Blanquat, M., Poujol, M., Boulvais, P., De Parseval, P., Rouleau, C., & Robert, J. F. (2016). Succession of Permian and Mesozoic metasomatic events in the eastern Pyrenees with emphasis on the Trimouns talc–chlorite deposit. *International Journal of Earth Sciences* **105**, 747-770.

Boynton, W. V. (1984). Cosmochemistry of the rare earth elements: meteorite studies. In *Developments in geochemistry* **2**, 63-114

Briand, B., Piboule, M. & Bouchardon, J.L. (1988). Diversité géochimique des métabasites des groupes leptyno-amphiboliques du Rouergue et de Marvejols (Massif central). Origine et implications. *Bull. Soc. Géol. France* **IV**, 489-498.

Brown, M. (2014). The contribution of metamorphic petrology to understanding lithosphere evolution and geodynamics. *Geoscience Frontiers* **5**, 553-569.

Burg, J. P., Leyreloup, A. F., Romney, F., & Delor, C. P. (1989). Inverted metamorphic zonation and Variscan thrust tectonics in the Rouergue area (Massif Central, France): PTt record from mineral to regional scale. *Geological Society, London, Special Publications* **43**, 423-439.

Brun, J.-P. & Faccenna, C., 2008. Exhumation of high-pressure rocks driven by slab rollback. *Earth and Planetary Science Letters*, **272**, 1-7.

Burg, J. P., & Teyssier, C. (1983). Contribution a l'étude tectonique et microtectonique des séries cristallophylliennes du Rouergue oriental: la déformation des laccolites syntectoniques, type Pinet. *Géologie de la France*, **1-2**, 3-29.

Butler, J. P., Jamieson, R. A., Dunning, G. R., Pecha, M. E., Robinson, P., & Steenkamp, H. M. (2018). Timing of metamorphism and exhumation in the Nordøyane ultra-high-pressure domain, Western Gneiss Region, Norway: New constraints from complementary CA-ID-TIMS and LA-MC-ICP-MS geochronology. *Lithos*, **310**, 153-170.

Capitani, C.D. & Petrakakis, K. (2010). The computation of equilibrium assemblage diagrams with Theriak/Domino software. *American Mineralogist* **95**, 1006-1016.

Carignan, J., Hild, P., Mevelle, G., Morel, J. & Yeghicheyan, D. (2001). Routine analyses of trace elements in geological samples using flow injection and low pressure on-line liquid chromatography coupled to ICP-MS: a study of geochemical reference materials BR, DR-N, UB-N, AN-G and GH. *Geostandards Newsletter* **25**, 187-198.

Chamberlain, K.R. & Bowring, S.A. (2001). Apatite–feldspar U–Pb thermochronometer: a reliable, mid-range (~ 450° C), diffusion-controlled system. *Chemical Geology* **172**, 173-200.

Chelle-Michou, C., Laurent, O., Moyen, J.F., Block, S., Paquette, J.L., Couzinié, S., Gardien, V., Vanderhaeghe, O., Villaros, A. & Zeh, A. (2017). Pre-Cadomian to late-Variscan odyssey of the eastern Massif Central, France: Formation of the West European crust in a nutshell. *Gondwana Research* **46**, 170-190.

Cheng, H., King, R. L., Nakamura, E., Vervoort, J. D., & Zhou, Z. (2008). Coupled Lu–Hf and Sm–Nd geochronology constrains garnet growth in ultra-high-pressure eclogites from the Dabie orogen. *Journal of Metamorphic Geology* **26**, 741-758.

Cheng, H., King, R. L., Nakamura, E., Vervoort, J. D., Zheng, Y. F., Ota, T., WU, Y.B., Katsura, K. & Zhou, Z. Y. (2009). Transitional time of oceanic to continental subduction in the Dabie orogen: constraints from U–Pb, Lu–Hf, Sm–Nd and Ar–Ar multichronometric dating. *Lithos*, **110**, 327-342.

Cheng, H., Zhang, C., Vervoort, J. D., Li, X., Li, Q., Wu, Y., & Zheng, S. (2012). Timing of eclogite facies metamorphism in the North Qinling by U–Pb and Lu–Hf geochronology. *Lithos*, **136**, 46-59.

Cherniak, D.J. (2000). Pb diffusion in rutile. *Contributions to Mineralogy and Petrology* **139**, 198-207.

Cherniak, D.J., Lanford, W.A. & Ryerson, F.J. (1991). Lead diffusion in apatite and zircon using ion implantation and Rutherford backscattering techniques. *Geochimica et Cosmochimica Acta* **55**, 1663-1673.

Chew, D.M., Petrus, J.A. & Kamber, B.S. (2014). U–Pb LA-ICPMS dating using accessory mineral standards with variable common Pb. *Chemical Geology* **363**, 185-199

Claiborne, L. L., Miller, C. F., Walker, B. A., Wooden, J. L., Mazdab, F. K., & Bea, F. (2006). Tracking magmatic processes through Zr/Hf ratios in rocks and Hf and Ti zoning in zircons: an example from the Spirit Mountain batholith, Nevada. *Mineralogical Magazine* **70**, 517-543.

Cochrane, R., Spikings, R.A., Chew, D., Wotzlaw, J.F., Chiaradia, M., Tyrrell, S., Schaltegger, U. & Van der Lelij, R. (2014). High temperature (> 350 C) thermochronology and mechanisms of Pb loss in apatite. *Geochimica et Cosmochimica Acta* **127**, 39-56.

Coggon, R. & Holland, T.J. (2002). Mixing properties of phengitic micas and revised garnet-phengite thermobarometers. *Journal of Metamorphic Geology* **20**, 683-96.

Collett, S., Štípská, P., Schulmann, K., Peřestý, V., Soldner, J., Anczkiewicz, R., Lexa, O. & Kylander-Clark, A. (2018). Combined Lu-Hf and Sm-Nd geochronology of the Mariánské Lázně Complex: New constraints on the timing of eclogite-and granulite-facies metamorphism. *Lithos*, **304**, 74-94.

Collomb, P. (1964). Etude géologique du Rouergue cristallin. Thèse d'Etat, Paris, 5 tomes.

Collomb, P. (1970). Etude géologique du Rouergue cristallin. *Mém. Expl. Serv. Carte géol. France,* Paris.

Couzinié, S., Moyen, J. F., Villaros, A., Paquette, J. L., Scarrow, J. H., & Marignac, C. (2014). Temporal relationships between Mg-K mafic magmatism and catastrophic melting of the Variscan crust in the southern part of Velay Complex (Massif Central, France). *Journal of Geosciences* **59**, 1-18.

Delbos, L., Lasserre, M. & Roques, M. (1964). Géochronologie et rétromorphose dans la série cristallophyllienne du Rouergue (Massif central français). *Sciences de la Terre* **10**, 329–342.

Del Greco, K., Johnston, S. T. & Shaw, J., (2016). Tectonic setting of the North Gondwana margin during the Early Ordovician: A comparison of the Ollo de Sapo and Famatina magmatic events. *Tectonophysics* **681**, 73-84.

Delor C., Leyreloup A. & Burg J.P. (1985). Nouveaux arguments pétrologiques enfaveur de l'allochtonie du Lévézou (Massif Central français): les enclaves basiques des granites calco-alcalins et les métacornéennes associées. *C. R. Acad. Sci. Paris* **301**, 1037–1042.

Diener, J.F. & Powell, R. (2012). Revised activity–composition models for clinopyroxene and amphibole. *Journal of Metamorphic Geology* **30**, 131-42.

Ducrot, J., Lancelot, J.R. & Marchand, J. (1983). Datation U-Pb sur zircons de l'éclogite de la Borie (Haut-Allier, France) et conséquences sur l'évolution anté-hercynienne de l'Europe occidentale. *Earth Planetary Science Letters* **18**, 97-113.

Duguet, M., & Faure, M. (2004). Granitoid emplacement during a thrusting event: structural analysis, microstructure and quartz c-axis patterns. An example from Hercynian plutons in the French Massif Central. *Journal of structural geology* **26**, 927-945.

Edel, J.B., Schulmann, K., Lexa, O., & Lardeaux, J.M. (2018). Late Palaeozoic palaeomagnetic and tectonic constraints for amalgamation of Pangea supercontinent in the European Variscan belt. *Earth-Science Reviews* **177**, 589-612.

Faure, M., Lardeaux, J.M. & Ledru, P. (2009). A review of the pre-Permian geology of the Variscan French Massif Central. *Comptes Rendus Geoscience* **341**, 202-13.

Forestier, F.H. (1971). Les schistes cristallins de la moitié nord duMassif Central. Symposium J. Jung: *Géologie, géomorphologie et structure profonde du Massif Central français* – Plein Air Serv. Ed. Clermont-Ferrand. 1971.

Franke, W. (2006). The Variscan orogen in Central Europe: construction and collapse. *Geological Society, London, Memoirs*, **32**, 333-343.

Gaggero, L., Oggiano, G., Funedda, A., & Buzzi, L. (2012). Rifting and arc-related early Paleozoic volcanism along the north Gondwana margin: Geochemical and geological evidence from Sardinia (Italy). *The Journal of Geology* **120**, 273-292.

García-Arias, M., Díez-Montes, A., Villaseca, C. & Blanco-Quintero, I. F. (2018). The Cambro-Ordovician Ollo de Sapo magmatism in the Iberian Massif and its Variscan evolution: A review. *Earth-Science Reviews* **176**, 345-372.

Gardien, V., Tegyey, E., Lardeaux, J. M., Misseri, M. & Dufour, E. (1990). Crust-mantle relationships in the French Variscan chain: the example of the Southern Monts du Lyonnais unit (eastern French Massif Central). *Journal of Metamorphic Geology* **8**, 477-492.

Grimes, C. B., John, B. E., Kelemen, P. B., Mazdab, F. K., Wooden, J. L., Cheadle, M. J., Hanghoj, K. & Schwartz, J. J. (2007). Trace element chemistry of zircons from oceanic crust: A method for distinguishing detrital zircon provenance. *Geology* **35**, 643-646.

Grimes, C. B., Wooden, J. L., Cheadle, M. J., & John, B. E. (2015). "Fingerprinting" tectono-magmatic provenance using trace elements in igneous zircon. *Contributions to Mineralogy and Petrology* **170**, 46.

Gutiérrez-Alonso, G., Gutiérrez-Marco, J.C., Fernández-Suárez, J., Bernárdez, E. & Corfu, F. (2016). Was there a super-eruption on the Gondwanan coast 477 Ma ago? *Tectonophysics* **681**, 85–94.

Harley, S.L., Kelly, N.M. & Möller, A. (2007). Zircon behaviour and the thermal histories of mountain chains. *Elements* **3**, 25-30.

Harrison, T.M., Catlos, E.J. & Montel, J.M. (2002). U-Th-Pb dating of phosphate minerals. *Reviews in Mineralogy and Geochemistry* **48**, 524-558.

Helbing, H., & Tiepolo, M. (2005). Age determination of Ordovician magmatism in NE Sardinia and its bearing on Variscan basement evolution. *Journal of the Geological Society* **162**, 689-700.

Holland, T., Baker, J. & Powell, R. (1998). Mixing properties and activity-composition relationships of chlorites in the system MgO-FeO-Al2O3-SiO2-H2O. *European Journal of Mineralogy* **22**, 395-406.

Holland, T. & Powell, R. (1998). An internally consistent thermodynamic data set for phases of petrological interest. *Journal of Metamorphic Geology* **16**, 309-43.

Holland, T. & Powell, R. (2003). Activity–composition relations for phases in petrological calculations: an asymmetric multicomponent formulation. *Contributions to Mineralogy and Petrology* **145**, 492-501.

Hollocher, K., Robinson, P., Walsh, E., & Roberts, D., (2012). Geochemistry of amphibolite-facies volcanics and gabbros of the Støren Nappe in extensions west and southwest of Trondheim, Western Gneiss Region, Norway: a key to correlations and paleotectonic settings. *American Journal of Science* **312**, 357-416.

Jackson, S.E., Pearson, N.J., Griffin, W.L. & Belousova, E.A. (2004). The application of laser ablation-inductively coupled plasma-mass spectrometry to in situ U–Pb zircon geochronology. *Chemical Geology* **211**, 47-69.

Janoušek, V., Farrow, C.M. & Erban, V. (2006). Interpretation of whole-rock geochemical data in igneous geochemistry: introducing Geochemical Data Toolkit (GCDkit). *Journal of Petrology* **47**, 1255-1259.

Jensen, L. S. (1976). A new cation plot for classifying subalkalic volcanic rocks. *Ministry of Natural Resources* **vol.66**.

Jochum, K.P., Weis, U., Stoll, B., Kuzmin, D., Yang, Q., Raczek, I., Jacob, D.E., Stracke, A., Birbaum, K., Frick, D.A. & Günther, D. (2011). Determination of reference values for NIST SRM 610–617 glasses following ISO guidelines. *Geostandards and Geoanalytical Research* **35**, 397-429.

Kooijman, E., Mezger, K. & Berndt, J. (2010). Constraints on the U–Pb systematics of metamorphic rutile from in situ LA-ICP-MS analysis. *Earth and Planetary Science Letters* **293**, 321-330.

Košler, J., Bowes, D.R., Konopásek, J., & Míková, J. (2004). Laser ablation ICPMS dating of zircons in Erzgebirge orthogneisses: evidence for Early Cambrian and Early Ordovician granitic plutonism in the western Bohemian Massif. *European Journal of Mineralogy* **16**, 15-22.

Kroner, U. & Romer, R. L. (2013). Two plates—many subduction zones: the Variscan orogeny reconsidered. *Gondwana Research* **24**, 298-329.

Kylander-Clark, A.R., Hacker, B.R., Johnson, C.M., Beard, B.L., Mahlen, N.J. & Lapen, T.J. (2007). Coupled Lu–Hf and Sm–Nd geochronology constrains prograde and exhumation

histories of high-and ultrahigh-pressure eclogites from western Norway. *Chemical Geology* **242**, 137-54.

Kylander-Clark, A.R.C., Hacker, B.R. & Mattinson, J.M. (2008). Slow exhumation of UHP terranes: titanite and rutile ages of the Western Gneiss Region, Norway. *Earth and Planetary Science Letters* **272**, 531-540.

Lardeaux, J.M. (2014). Deciphering orogeny: a metamorphic perspective Examples from European Alpine and Variscan belts Part II: Variscan metamorphism in the French Massif Central—a review. *Bulletin de la Société Géologique de France* **185**, 281-310.

Lardeaux, J. M., Schulmann, K., Faure, M., Janoušek, V., Lexa, O., Skrzypek, E., Edel, J. B. & Štípská (2014). The Moldanubian Zone in the Fench Massif Central/Vosges/Schwartzwald and Bohemina Massif revisited: differences and similarities. *Geological Society, London, Special Publication* 405, 7-44.

Lardeaux, J. M., Ledru, P., Daniel, I. & Duchêne, S. (2001). The Variscan French Massif Central—a new addition to the ultra-high pressure metamorphic 'club': exhumation processes and geodynamic consequences. *Tectonophysics* **332**, 143-167.

Lasnier, B. (1970). Le métamorphisme régional des gabbros d'après la littérature internationale: étude préliminaire des gabbros coronitiques du Massif Armoricain et du Massif des Maures (France). *Thesis,* University of Nantes, 295 pp

Lasnier, B. (1977). Persistance d'une série granulitique au coeur du Massif central français (Haut-Allier). Les termes basiques, ultrabasiques et carbonatés. Thèse d'Etat, Univ. Nantes, 351 p.

Laurent, O., Couzinié, S., Zeh, A., Vanderhaeghe, O., Moyen, J. F., Villaros, A., Gardien, V. & Chelle-Michou, C. (2017). Protracted, coeval crust and mantle melting during Variscan

late-orogenic evolution: U–Pb dating in the eastern French Massif Central. *International Journal of Earth Sciences*, **106**, 421-451.

Leake, B.E., Woolley, A.R., Arps, C.E., Birch, W.D., Gilbert, M.C., Grice, J.D., Hawthorne, F.C., Kato, A., Kisch, H.J., Krivovichev, V.G. & Linthout, K. (1997). Report Nomenclature of Amphiboles: Report of the Subcommittee on Amphiboles of the International Mineralogical Association Commission on New Minerals and Mineral Names. *Mineralogical Magazine* **61**, 295-321.

Leeder, M. R. (1991). Denudation, vertical crustal movements and sedimentary basin infill. *Geologische Rundschau*, **80**, 441-458.

Ledru, P., Lardeaux, J.M., Santallier, D., Autran, A., Quenardel, J.M., Floc'h, J.P., Lerouge, G., Maillet, N., Marchand, J. & Ploquin, A. (1989). Où sont les nappes dans le Massif Central Français? *Bulletin de la Société Géolgique de France* **3**, 605–618.

Linnemann, U., Pereira, F., Jeffries, T.E., Drost, K., & Gerdes, A. (2008). The Cadomian Orogeny and the opening of the Rheic Ocean: the diacrony of geotectonic processes constrained by LA-ICP-MS U–Pb zircon dating (Ossa-Morena and Saxo-Thuringian Zones, Iberian and Bohemian Massifs). *Tectonophysics* **461**, 21-43.

Lotout, C. (2017). Age, durée et enregistrement du métamorphisme de haute pression dans le Massif Central, chaîne Varisque. *PhD thesis*, University of Rennes, 374pp.

Lotout, C., Pitra, P., Poujol, M. & Van Den Driessche, J. (2017). Ordovician magmatism in the Lévézou massif (French Massif Central): tectonic and geodynamic implications. *International Journal of Earth Sciences* **106**, 501-515.

Lotout, C., Pitra, P., Poujol, M., Anczkiewicz, R., & Van Den Driessche, J. (2018). Timing and duration of Variscan high-pressure metamorphism in the French Massif Central: A multimethod geochronological study from the Najac Massif. *Lithos*, **308**, 381-394.

Ludwig, K.R. (2012). User's Manual for a geochronological toolkit for Microsoft Excel. *Berkeley Geochronological* Center 75.

Lugmair, G.W. & Marti, K. (1978). Lunar initial $^{143}Nd/^{144}Nd$: differential evolution of the lunar crust and mantle. *Earth and Planetary Science Letters* **39**, 349-357.

Manzotti, P., Bosse, V., Pitra, P., Robyr, M., Schiavi, F., & Ballèvre, M. (2018). Exhumation rates in the Gran Paradiso Massif (Western Alps) constrained by in situ U–Th–Pb dating of accessory phases (monazite, allanite and xenotime). *Contrib. Mineral. Petrol*. **173**, 24.

Martínez Catalán, J.R., Arenas, R., Abati, J., Martínez, S.S., García, F.D., Suárez, J.F., Cuadra, P.G., Castiñeiras, P., Barreiro, J.G., Montes, A.D. & Clavijo, E.G. (2009). A rootless suture and the loss of the roots of a mountain chain: the Variscan belt of NW Iberia. *Comptes Rendus Geoscience* **341**, 114-126.

Mattauer, M. (1986). Intracontinental subduction, crust-mantle décollement and crustal stacking wedge in the Himalayas and other collision belts. *Geological Society, London, Special Publication* **19**, 37-50.

Matte, P. (1986). Tectonics and plate tectonics model for the Variscan belt of Europe. *Tectonophysics* **126**, 329-374.

Matte, P., & Burg, J.P. (1981). Sutures, thrusts and nappes in the Variscan Arc of western Europe: plate tectonic implications. *Geological Society, London, Special Publications* **9**, 353-358.

McDowell, F.W., McIntosh, W.C. & Farley, K.A. (2005). A precise 40Ar–39Ar reference age for the Durango apatite (U–Th)/He and fission-track dating standard. *Chemical Geology* **214**, 249-263.

Mezger, K., Hanson, G.N. & Bohlen S.R. (1989). High-precision U–Pb ages of metamorphic rutile: application to the cooling history of high-grade terranes. *Earth and Planetary Science Letters* **96**, 106–118.

Mezger, K., Rawnsley, C.M., Bohlen, S.R. & Hanson, G.N. (1991). U-Pb garnet, sphene, monazite, and rutile ages: implications for the duration of high-grade metamorphism and cooling histories, Adirondack Mts., New York. *The Journal of Geology* **99**, 15-428.

Murphy, J. B., Nance, R. D., & Cawood, P. A. (2009). Contrasting modes of supercontinent formation and the conundrum of Pangea. *Gondwana Research* **15**, 408-420.

Nicollet, C. (1978). Pétrologie et tectonique des terrains cristallins antépermiens du versant sud du dôme du Lévezou (Rouergue, Massif central). *Bull BRGM* **3**, 225–263.

Nicollet, C. & Leyreloup, A. (1978). Pétrologie des niveaux trondhjemitiques de haute pression et de leur encaissant éclogitique et amphibolitique (Levezou et Marvejols, Massif Central Francais). Conséquences sur la génèse des groupes leptyno-amphibolitiques. *Can. Journal of Earth Sciences* **15**, 696-707.

Oggiano, G., Gaggero, L., Funedda, A., Buzzi, L., & Tiepolo, M. (2010). Multiple early Paleozoic volcanic events at the northern Gondwana margin: U–Pb age evidence from the Southern Variscan branch (Sardinia, Italy). *Gondwana Research* **17**, 44-58.

Palin, R. M., Weller, O. M., Waters, D. J. & Dyck, B., 2016. Quantifying geological uncertainty in metamorphic phase equilibria modelling; a Monte Carlo assessment and implications for tectonic interpretations. *Geoscience Frontiers* **7**, 591-607.

Paquette, J. L., Ballèvre, M., Peucat, J. J., & Cornen, G. (2017). From opening to subduction of an oceanic domain constrained by LA-ICP-MS U-Pb zircon dating (Variscan belt, Southern Armorican Massif, France). *Lithos* **294**, 418-437.

Paquette, J.L., Monchoux, P. & Couturier, M. (1995). Geochemical and isotopic study of a norite-eclogite transition in the European Variscan Belt: Implications for U-Pb zircon systematics in metabasic rocks. *Geochim. Cosmochim. acta* **59**, 1611-1622.

Paton, C., Woodhead, J.D., Hellstrom, J.C., Hergt, J.M., Greig, A. & Maas, R. (2010). Improved laser ablation U-Pb zircon geochronology through robust downhole fractionation correction. *Geochemistry, Geophysics, Geosystems*, **11,** Q0AA06, doi:10.1029/2009GC002618.

Pearce, J. A. (1996). A user's guide to basalt discrimination diagrams. Trace element geochemistry of volcanic rocks: applications for massive sulphide exploration. *Geological Association of Canada, Short Course Notes* **12**, 79-113.

Pearce, J.A. (2008). Geochemical fingerprinting of oceanic basalts with applications to ophiolite classification and the search for Archean oceanic crust. *Lithos* **100**, 14-48.

Pearce, J. A., & Cann, J. R. (1971). Ophiolite origin investigated by discriminant analysis using Ti, Zr and Y. *Earth and Planetary Science Letters* **12**, 339-349.

Piboule, M. (1979). L'origine des amphibolites: approche géochimique et mathématique. Application aux amphibolites du Massif central français. Thèse d'Etat, Lyon I University

Piboule, M. & Briand, B., (1985). Geochemistry of eclogites and associated rocks of the southeastern area of the French Massif Central: origin of the protoliths. *Chemical geology* **50**, 189-99.

Pin, C. (1979). Géochronologie U–Pb et microtectonique des séries métamorphiques anté-stéphaniennes de l'Aubrac et de la région de Marvejols (Massif central). PhD Thesis, Montpellier University

Pin, C. (1990). Variscan oceans: ages, origins and geodynamic implications inferred from geochemical and radiometric data. *Tectonophysics* **177**, 215-227.

Pin, C. & Piboule, M. (1988). Upper Devonian U–Pb zircon age of the calc-alkaline series in the Levezou mafic belt, Rouergue (Massif Central, France). A composite leptyno-amphibolitic association. *Bull Soc Géol Fr* **4**, 261–265

Pin, C. & Lancelot, J. (1982). U–Pb dating of an early Paleozoic bimodal magmatism in the French Massif Central and its further metamorphic evolution. *Contribution to Mineralogy and Petrology* **79**, 1-12.

Pitra, P. & de Waal, S. A. (2001). High-temperature, low-pressure metamorphism and development of prograde symplectites, Marble Hall Fragment, Bushveld Complex (South Africa). *Journal of Metamorphic Geology* **19**, 311-325.

Pitra, P., Boulvais, P., Antonoff, V. & Diot, H. (2008). Wagnerite in a cordierite-gedrite gneiss: Witness of long-term fluid-rock interaction in the continental crust (Ile d'Yeu, Armorican Massif, France). *American Mineralogist* **93**, 315-26.

Pitra, P., Poujol, M., Van Den Driessche, J., Poilvet, J.-C., Paquette, J.-L. (2012). Early Permian extensional shearing of an Ordovician granite: The Saint-Eutrope ,"C/S-like" orthogneiss (Montagne Noire, French Massif Central). *Comptes Rendus Geoscience*, **344** 377-384.

Pochon, A., Poujol, M., Gloaguen, E., Branquet, Y., Cagnard, F., Gumiaux, C. & Gapais, D. (2016). U-Pb LA-ICP-MS dating of apatite in mafic rocks: Evidence for a major

magmatic event at the Devonian-Carboniferous boundary in the Armorican Massif (France). *American Mineralogist* **101**, 2430-2442.

Ribeiro, A., Munhá, J., Dias, R., Mateus, A., Pereira, E., Ribeiro, L., Fonseca, P., Araujo, A., Oliveira, T., Rosmao, J., Chaminé, H., Coke, C. & Pedro, J. (2007). Geodynamic evolution of the SW Europe Variscides. *Tectonics* **26**.

Rubatto, D. (2002). Zircon trace element geochemistry: partitioning with garnet and the link between U–Pb ages and metamorphism. *Chemical geology* **184**, 123-38.

Sánchez-Garcıa, T., Bellido, F., & Quesada, C. (2003). Geodynamic setting and geochemical signatures of Cambrian–Ordovician rift-related igneous rocks (Ossa-Morena Zone, SW Iberia). *Tectonophysics* **365**, 233-255.

Sánchez-García, T., Quesada, C., Bellido, F., Dunning, G. R., & Del Tánago, J. G. (2008). Two-step magma flooding of the upper crust during rifting: the Early Paleozoic of the Ossa Morena Zone (SW Iberia). *Tectonophysics* **461**, 72-90.

Santallier, D.A., Briand, B.E., Menot, R.P. & Piboule, M. (1988). Les complexes leptyno-amphiboliques (CLA): revue critique et suggestions pour un meilleur emploi de ce terme. *Bulletin de la Société Géologique de France* **1**, 3-12.

Scherer, E., Münker, C. & Mezger, K. (2001). Calibration of the lutetium-hafnium clock. *Science* **293**, 683-687.

Schoene, B. & Bowring, S.A. (2006). U–Pb systematics of the McClure Mountain syenite: Thermochronological constraints on the age of the 40Ar/39Ar standard MMhb. *Contributions to Mineralogy and Petrology* **151**, 615–630.

Schoene, B. & Bowring, S.A. (2007) Determining accurate temperature–time paths from U–Pb thermochronology: An example from the Kaapvaal craton, southern Africa. *Geochimica et Cosmochimica Acta* **71**,165–185.

Schulmann, K., Catalán, J.R.M., Lardeaux, J. M., Janoušek, V., & Oggiano, G. (2014). The Variscan orogeny: extent, timescale and the formation of the European crust. *Geological Society, London, Special Publications* **405**, 1-6.

Sláma, J., Košler, J., Condon, D.J., Crowley, J.L., Gerdes, A., Hanchar, J.M., Horstwood, M.S., Morris, G.A., Nasdala, L., Norberg, N. & Schaltegger, U. (2008). Plešovice zircon—a new natural reference material for U–Pb and Hf isotopic microanalysis. *Chemical Geology* **249**, 1-35.

Smit, M.A., Scherer, E.E. & Mezger, K. (2013). Lu–Hf and Sm–Nd garnet geochronology: Chronometric closure and implications for dating petrological processes. *Earth and Planetary Science Letters* **381**, 222-33.

Stacey, J.T. & Kramers, J.D. (1975). Approximation of terrestrial lead isotope evolution by a two-stage model. *Earth and planetary science letters* **26**, 207-21.

Sun, S.S. & McDonough, W.F. (1989). Chemical and isotopic systematics of oceanic basalts: implications for mantle composition and processes. *Geological Society, London, Special Publications* **42**, 313-345.

Taylor, R.J.M., Clark, C., Harley, S. L., Kylander-Clark, A.R.C., Hacker, B.R. & Kinny, P. D. (2017). Interpreting granulite facies events through rare earth element partitioning arrays. *Journal of Metamorphic Geology* **35**, 759-775.

Tirone, M., Ganguly, J., Dohmen, R., Langenhorst, F., Hervig, R., & Becker, H. W. (2005). Rare earth diffusion kinetics in garnet: experimental studies and applications. *Geochimica et Cosmochimica Acta* **69**, 2385-2398.

Thirlwall, M.F. & Anczkiewicz, R. (2004). Multidynamic isotope ratio analysis using MC–ICP–MS and the causes of secular drift in Hf, Nd and Pb isotope ratios. *International Journal of Mass Spectrometry* **235**, 59-81.

Van Achterbergh, E., Ryan, C.G., Jackson, S.E. & Griffin, W.L. (2001). Data reduction software for LA-ICP-MS: appendix. In: Laser Ablation-ICP-Mass Spectrometry in the Earth Sciences: Principles and Applications. In Mineralog Assoc Canada (MAC) Short Courses Series (Sylvester, P.J., eds), Ottawa, Ontario, Canada 29, 239-243.

Verma, S.P., Guevara, M., & Agrawal, S., (2006). Discriminating four tectonic settings: Five new geochemical diagrams for basic and ultrabasic volcanic rocks based on log—ratio transformation of major-element data. *Journal of Earth System Science* **115**, 485-528.

Villaseca, C., Castiñeiras, P. & Orejana, D., (2015). Early Ordovician metabasites from the Spanish Central System: A remnant of intraplate HP rocks in the Central Iberian Zone. *Gondwana Research* **27**, 392-409.

Vry, J. K., & Baker, J. A. (2006). LA-MC-ICPMS Pb–Pb dating of rutile from slowly cooled granulites: confirmation of the high closure temperature for Pb diffusion in rutile. *Geochimica et Cosmochimica Acta* **70**, 1807-1820.

Walczak, K., Anczkiewicz, R., Szczepanski, J., Rubatto, D. & Kosler, J., (2017). Combined garnet and zircon geochronology of the ultra-high temperature metamorphism: Constraints on the rise of the Orlica-Snieznik Dome, NE Bohemian Massif, SW Poland. *Lithos* **292**, 388-400.

Warren, C.J., Grujic, D., Cottle, J.M. & Rogers, N.W. (2012). Constraining cooling histories: rutile and titanite chronology and diffusion modelling in NW Bhutan. *Journal of Metamorphic Geology* **30**, 113-30.

White, R.W., Powell, R., Holland, T.J. & Worley, B.A. (2000). The effect of TiO~ 2 and Fe~ 2O~ 3 on metapelitic assemblages at greenschist and amphibolite facies conditions: mineral equilibria calculations in the system The effect of TiO2 and Fe2O3 on metapelitic assemblages at greenschist and amphibolite facies conditions: mineral equilibria calculations in the system K2O–FeO–MgO–Al2O3–SiO2–H2O–TiO2–Fe2O3. *Journal of Metamorphic Geology* **18**, 497-512.

White R.W., Powell R. & Holland T.J. (2007). Progress relating to calculation of partial melting equilibria for metapelites. *Journal of Metamorphic Geology* **25**, 511-27.

Whitehouse, M.J. Platt, J.P. (2003). Dating high-grade metamorphism—constraints from rare-earth elements in zircon and garnet. *Contributions to Mineralogy and Petrology* **145**, 61-74.

Wood, D. A. (1980). The application of a ThHfTa diagram to problems of tectonomagmatic classification and to establishing the nature of crustal contamination of basaltic lavas of the British Tertiary Volcanic Province. *Earth and planetary science letters* **50**, 11-30.

Woodhead, J.D., Hellstrom, J., Hergt, J.M., Greig, A. & Maas, R., (2007). Isotopic and elemental imaging of geological materials by laser ablation inductively coupled plasma-mass spectrometry. *Geostandards and Geoanalytical Research* **31**, 331-343.

Zack, T., Moraes, R., & Kronz, A., (2004). Temperature dependence of Zr in rutile: empirical calibration of a rutile thermometer. *Contributions to Mineralogy and Petrology* **148**, 471-488.

Zack, T., Stockli, D.F., Luvizotto, G.L., Barth, M.G., Belousova, E., Wolfe, M.R., & Hinton, R.W., (2011). In situ U–Pb rutile dating by LA-ICP-MS: 208 Pb correction and prospects for geological applications. *Contributions to Mineralogy and Petrology* **162**, 515-530.

Figure captions

Figure 1: (a) Schematic map of the Leptyno-Amphibolitic Complex (LAC) outcrops in the French Massif Central, with the location of the study area and the previous geochronological studies. (1) Pin & Lancelot, 1982 (U-Pb, zircon isotopic dilution), (2) Ducrot *et al*., 1983 (U-Pb, zircon isotopic dilution), (3) Paquette *et al*., 1995 (Sm-Nd - garnet and WR), (4) Berger *et al*., 2010 (U-Pb, LA-ICP-MS dating on zircon), (5) Lotout *et al*., 2018 (U-Pb, LA-ICP-MS dating on zircon; Lu-Hf and Sm-Nd dating on garnet). Inset shows the location of the study area within the European Variscan belt A - Alps, AM - Armorican Massif, BM - Bohemian Massif, FMC – French Massif Central. B - Teplá-Barrandian, Mo - Moldanubian, ST - Saxothuringian, RH – Rhenohercynian. (b) Schematic map of the Lévézou massif (modified after Lotout *et al*., 2017). D1 and D2 thrusting according to Duguet & Faure (2004). Purple stars indicate the samples location; see the text for the exact GPS coordinates.

Figure 2: Whole-rock composition diagrams of samples LV21 (blue crosses) and LV20B (orange circles). (a) REE normalised to chondrite (Boynton 1984), (b) Zr/Ti vs Nb/Y after Pearce (1996), (c) spider diagram normalized to NMORB immobile elements (Sun & McDonough, 1989), (d) diagram Al - (Fe^T + Ti) - Mg after Jensen (1976), used abbreviation: TH – tholeiitic serie, CA – calc-alkaline serie.

Figure 3: Sample LV21. Photomicrographs (plane polarized light) (a) and X-ray maps for Ca (b) and Fe (c). Abbreviations are described in the Analytical Procedures section.

Figure 4: Compositional diagrams of clinopyroxene (a), garnet (b) and amphibole (c, d). (e, f) Compositional profiles of garnet. Results are colour-coded according to the sample. Amphibole nomenclature follows the classification of Leake *et al*. (1997). Abbreviations are described in the Analytical Procedures section.

Figure 5: P–T pseudosection for the sample LV21 calculated with H_2O saturation and 8.2% Fe^{3+} (of total iron), corresponding to the analyzed amount. The rock composition, given as mol.% oxide, is SiO_2(48.87)–TiO_2(0.57)–Al_2O_3(11.71)–Fe_2O_3(0.24)–FeO(5.24)–MgO(18.22)–CaO(12.55)–Na_2O(2.49). Fields are coloured with respect to their variance, darker colours indicate lower variance assemblage. Rutile and an aqueous fluid (H2O) are present in all fields.. The peak high-pressure assemblage is highlighted (a). Modelled compositional isopleths for X_{Mg} of garnet and amphibole (b), and grossular (X_{Grs}) in garnet (c) with bold lines marking the observed range. Mode isopleths for garnet (c) show that garnet can only grow along a prograde P–T path. Abbreviations are described in the Analytical Procedures section.

Figure 6: Photomicrographs of the sample LV20B (plane polarized light) (a-c) and X-ray maps for Mn (d), Ca (e) and Mg (f). Clinopyroxene has the chemical composition of diopside. Abbreviations are described in the Analytical Procedures section.

Figure 7: P–T pseudosection for the sample LV20B, calculated with H_2O saturation and 13.3% Fe^{3+} (of total iron), corresponding to the analysed amount. The rock composition, given as mol.% oxide, is SiO_2(54.26)–TiO_2(0.82)–Al_2O_3(9.18)–Fe_2O_3(0.53)–FeO(6.95)–MgO(13.65)–CaO(11.68)- K_2O(0.99)–Na_2O(2.42). Fields are coloured with respect to their variance, darker colours indicate lower variance assemblages. Aqueous fluid (H_2O) is present in all fields. The peak high-pressure assemblage is highlighted. Curved lines on the left part of the P–T pseudosection correspond to amphibole solvi

(a). (b) Modelled compositional isopleths for garnet (X_{Mg}) and amphibole (Si), with bold lines marking the observed range. (c) Modelled compositional isopleths for plagioclase (X_{Ab}) and amphibole (Si), with bold lines marking the observed range. Abbreviations are described in the Analytical Procedures section.

Figure 8: Trace element profiles for garnet from samples LV21 (a, c) and LV20B (b, d).

Figure 9: Lu–Hf (a, b) and Sm–Nd (c, d) isochron diagrams for samples LV21 and LV20B. WR – whole rock, grt – garnet, 1-3 – garnet fractions, amph – amphibole, cpx – clinopyroxene. Errors of Lu-Hf analyses were too small to be visible, consequently data points were increased.

Figure 10: Selected cathodoluminescence images of zircon crystals, displaying the various textures observed. White (35 and 25 μm) circles show the location of the U-Pb analyses and the corresponding analysis number.

Figure 11: Tera–Wasserburg ($^{207}Pb/^{206}Pb$ vs. $^{238}U/^{206}Pb$) diagrams displaying all dates obtained on zircon (a), concordant Cambrian analyses (b), concordant Ordovician analyses (c), and all Devonian analyses with the Concordia age in insert (d).

Figure 12: Trace element chemistry for dated zircons. (a) REE content normalized to chondrite for zircon displaying Devonian dates (blue), Ordovician dates (green), Cambrian dates (orange). (b) Y (ppm) vs. Eu/Eu* anomaly diagram, with the recorded dates colour-coded accordingly. (c) U/Yb vs. Hf and (d) U/Yb vs. Y discriminant geotectonic diagrams (Grimes *et al*., 2007). (e) Gd/Yb vs. Ce/Yb and (f) U/Yb vs. Gd/Yb petrogenetic diagram for zircon (Grimes *et al*., 2015). See text for details.

Figure 13: Tera–Wasserburg ($^{207}Pb/^{206}Pb$ vs. $^{238}U/^{206}Pb$) diagram displaying all dates obtained on rutile from LV21 (a) and LV20B (b) and apatite from LV20B (c) and the mean age ^{207}Pb-corrected (d).

Figure 14: P–T (a) and Age – Temperature (b) diagram summarizing the chronological and petrological results from this study.

Figure 15: Ages of high-pressure metamorphic rocks in the European Variscan belt, (modified after Paquette *et al*., 2017). Result from this study is highlighted.

Table 1: Summary of the Lu–Hf and Sm–Nd dating results.

Footnote to Table 1: All errors are 2 se (standard errors) and relate to the last significant digits. $^{176}Lu/^{177}Hf$ errors are 0.5% and $^{147}Sm/^{144}Nd$ errors are 0.3%. Reproducibility of JMC475 yielded 0.282166 ± 4 (N = 4) over the period of analyses, while JNd^{-1} gave 0.512098 ± 5 (N = 7). Hf and Nd mass bias were corrected to $^{179}Hf/^{177}Hf = 0.7325$ and $^{146}Nd/^{144}Nd = 0.7219$, respectively. Decay constants applied to age calculations: $\lambda^{176}Lu = 1.865x10^{-11}$ yr^{-1} (Scherer et al., 2001) and $\lambda^{147}Sm = 6.54x10^{-12}$ yr^{-1} (Lugmair and Marti, 1978). Procedure blanks for all elements were below 30 pg.

Supplementary Figure 1: Whole-rock composition diagrams of samples LV21 (blue crosses) and LV20B (orange circles). Geotectonic discrimation diagrams for basic and ultrabasic rocks (Verma *et al*., 2006); island arc basic rocks (IAB), continental rift basic rocks (CRB), ocean-island basic rocks (OIB), and mid-ocean ridge basic rocks (MORB).

Supplementary Figure 2: Whole-rock composition diagrams of samples LV21 (blue crosses) and LV20B (orange circles). (a) Nb/La vs. La/Yb geotectonic diagrams (Hollocher *et al.*, 2012), (b) Th/Yb vs Nb/Yb (Pearce, 2008).

Supplementary Figure 3: P–T pseudosection for the sample LV21 calculated with H_2O saturation, 8.2% Fe^{3+} (of total iron, corresponding to the analyzed amount) and modelled compositional isopleths for X_{Mg} and X_{Jd} of clinopyroxene. The rock composition, given as mol.% oxide, is SiO_2(48.87)–TiO_2(0.57)–Al_2O_3(11.71)–Fe_2O_3(0.24)–FeO(5.24)–MgO(18.22)–CaO(12.55)–Na_2O(2.49). Fields are coloured with respect to their variance, darker colours indicate lower variance assemblage. The peak high-pressure assemblage is highlighted. See Figure 5 for mineral assemblages and other isopleths.

Supplementary Table 1: Operating conditions for the LA-ICP-MS equipment

Supplementary Table 2: Summary of the U-Pb LA-ICP-MS analyses in zircon, rutile and apatite

Supplementary Table 3: Whole-rock chemical compositions of the samples LV21 and LV20B. LOI: Loss on ignition; Bdl: below detection limit, Fe2O3 corresponds to total Fe; FeO to Fe2+ only, analyzed by titration.

Supplementary Table 4: Representative microprobe analyses of principal metamorphic minerals. The amount of ferric iron was calculated from stoichiometric constraints.

Supplementary Table 5: Non-exhaustive summary of the trace element analyses in garnet. Trace element contents are normalized to chondrite after Boyton (1984). Bdl: below detection limit.

Supplementary Table 6: Summary of the trace element analyses in zircon, with the analyzed age range specified. Trace element contents are normalized to chondrite after Sun and McDonough (1989). Bdl: below detection limit.

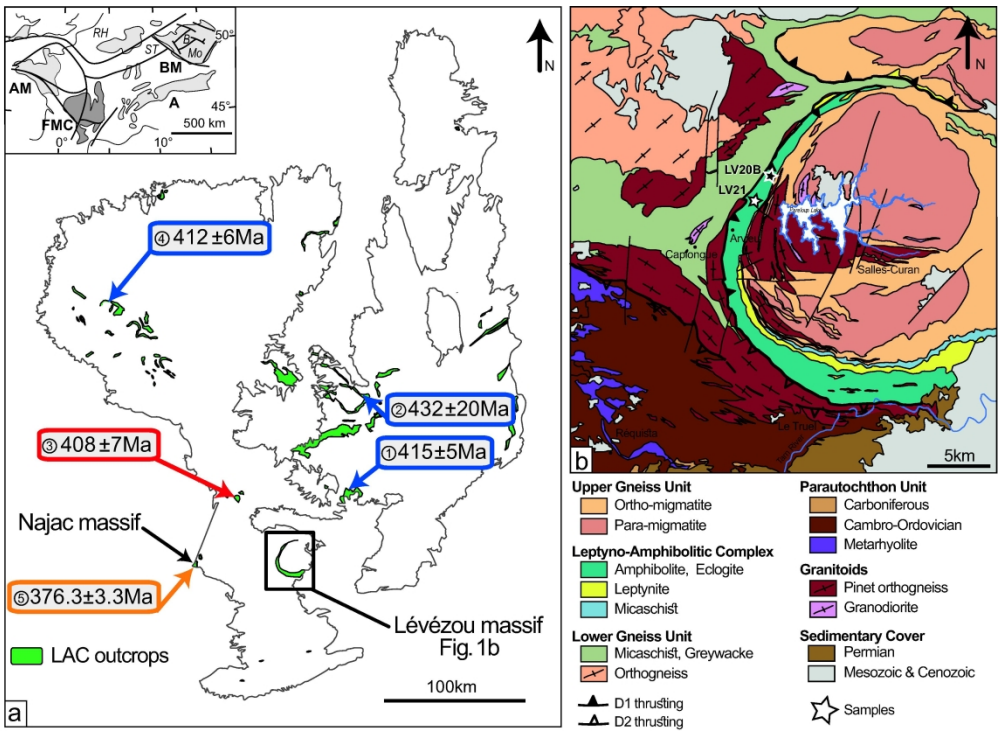

Figure 1: (a) Schematic map of the Leptyno-Amphibolitic Complex (LAC) outcrops in the French Massif Central, with the location of the study area and the previous geochronological studies. (1) Pin & Lancelot, 1982 (U-Pb, zircon isotopic dilution), (2) Ducrot et al., 1983 (U-Pb, zircon isotopic dilution), (3) Paquette et al., 1995 (Sm-Nd - garnet and WR), (4) Berger et al., 2010 (U-Pb, LA-ICP-MS dating on zircon), (5) Lotout et al., 2018 (U-Pb, LA-ICP-MS dating on zircon; Lu-Hf and Sm-Nd dating on garnet). Inset shows the location of the study area within the European Variscan belt A - Alps, AM - Armorican Massif, BM - Bohemian Massif, FMC – French Massif Central. B - Teplá-Barrandian, Mo - Moldanubian, ST - Saxothuringian, RH – Rhenohercynian. (b) Schematic map of the Lévézou massif (modified after Lotout et al., 2017). D1 and D2 thrusting according to Duguet & Faure (2004). Purple stars indicate the samples location; see the text for the exact GPS coordinates.

166x120mm (600 x 600 DPI)

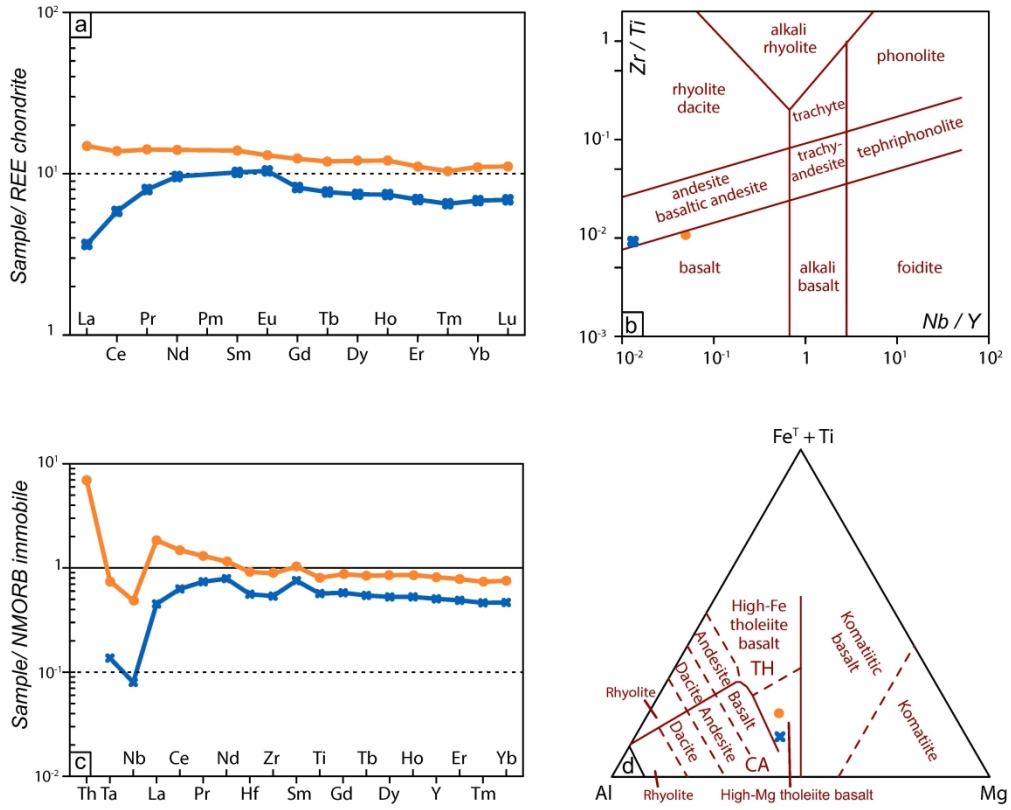

Figure 2: Whole-rock composition diagrams of samples LV21 (blue crosses) and LV20B (orange circles). (a) REE normalised to chondrite (Boynton 1984), (b) Zr/Ti vs Nb/Y after Pearce (1996), (c) spider diagram normalized to NMORB immobile elements (Sun & McDonough, 1989), (d) diagram Al - (FeT + Ti) - Mg after Jensen (1976), used abbreviation: TH – tholeiitic serie, CA – calc-alkaline serie.

168x136mm (600 x 600 DPI)

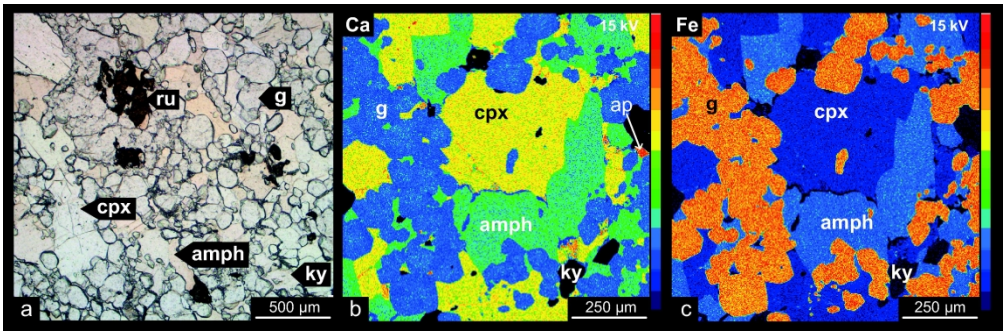

Figure 3: Sample LV21. Photomicrographs (plane polarized light) (a) and X-ray maps for Ca (b) and Fe (c). Abbreviations are described in the Analytical Procedures section.

176x57mm (600 x 600 DPI)

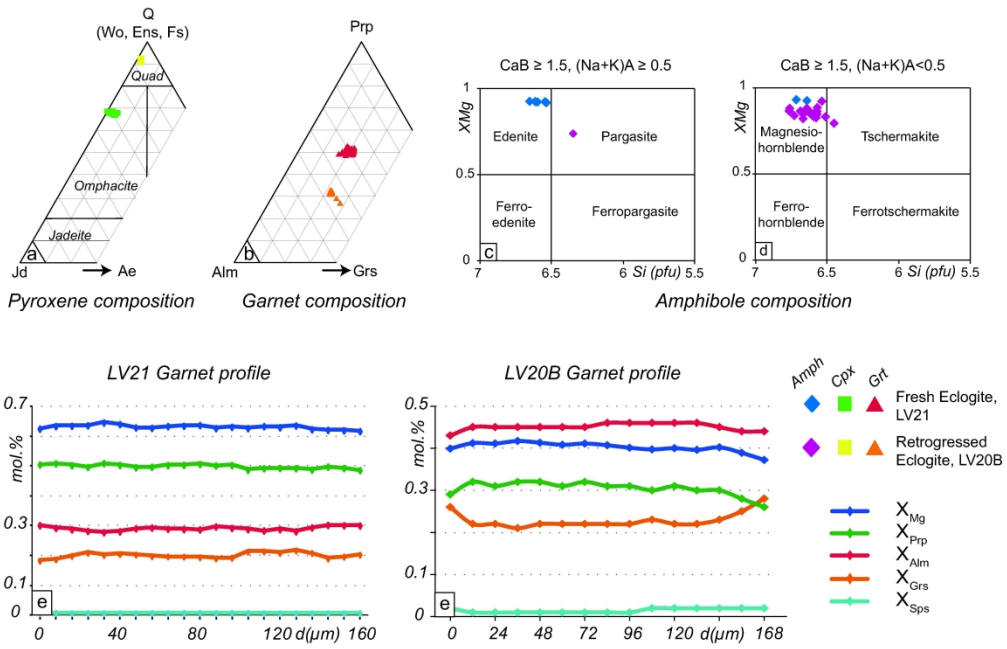

Figure 4: Compositional diagrams of clinopyroxene (a), garnet (b) and amphibole (c, d). (e, f) Compositional profiles of garnet. Results are colour-coded according to the sample. Amphibole nomenclature follows the classification of Leake et al. (1997). Abbreviations are described in the Analytical Procedures section.

185x118mm (600 x 600 DPI)

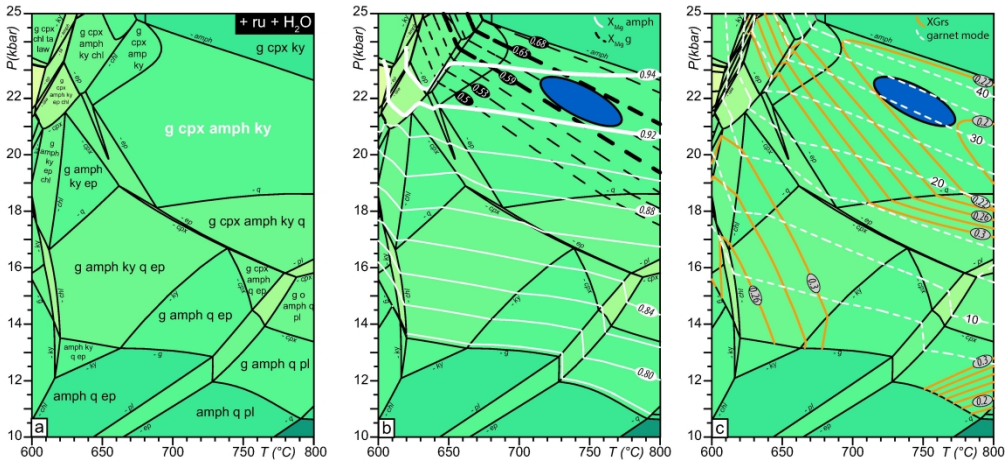

Figure 5: P–T pseudosection for the sample LV21 calculated with H2O saturation and 8.2% Fe3+ (of total iron), corresponding to the analyzed amount. The rock composition, given as mol.% oxide, is SiO2(48.87)–TiO2(0.57)–Al2O3(11.71)–Fe2O3(0.24)–FeO(5.24)–MgO(18.22)–CaO(12.55)–Na2O(2.49). Fields are coloured with respect to their variance, darker colours indicate lower variance assemblage. Rutile and an aqueous fluid (H2O) are present in all fields.. The peak high-pressure assemblage is highlighted (a). Modelled compositional isopleths for XMg of garnet and amphibole (b), and grossular (XGrs) in garnet (c) with bold lines marking the observed range. Mode isopleths for garnet (c) show that garnet can only grow along a prograde P–T path. Abbreviations are described in the Analytical Procedures section.

183x83mm (600 x 600 DPI)

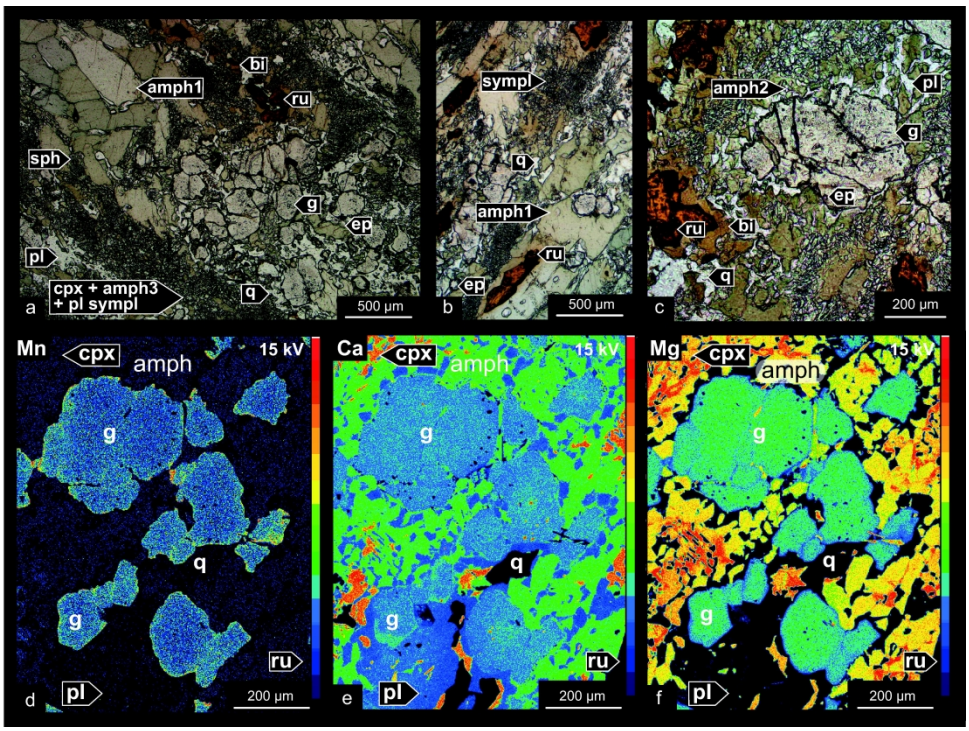

Figure 6: Photomicrographs of the sample LV20B (plane polarized light) (a-c) and X-ray maps for Mn (d), Ca (e) and Mg (f). Clinopyroxene has the chemical composition of diopside. Abbreviations are described in the Analytical Procedures section.

204x147mm (600 x 600 DPI)

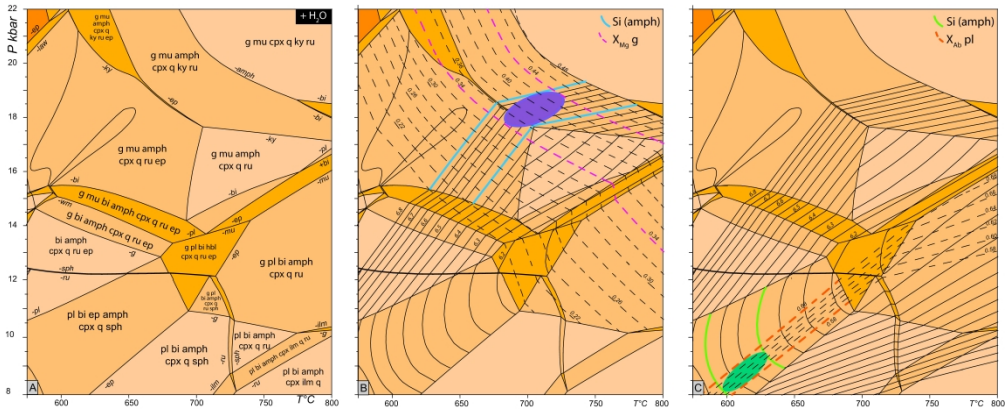

Figure 7: P–T pseudosection for the sample LV20B, calculated with H2O saturation and 13.3% Fe3+ (of total iron), corresponding to the analysed amount. The rock composition, given as mol.% oxide, is SiO2(54.26)–TiO2(0.82)–Al2O3(9.18)–Fe2O3(0.53)–FeO(6.95)–MgO(13.65)–CaO(11.68)- K2O(0.99)–Na2O(2.42). Fields are coloured with respect to their variance, darker colours indicate lower variance assemblages. Aqueous fluid (H2O) is present in all fields. The peak high-pressure assemblage is highlighted. Curved lines on the left part of the P–T pseudosection correspond to amphibole solvi (a). (b) Modelled compositional isopleths for garnet (XMg) and amphibole (Si), with bold lines marking the observed range. (c) Modelled compositional isopleths for plagioclase (XAb) and amphibole (Si), with bold lines marking the observed range. Abbreviations are described in the Analytical Procedures section.

554x224mm (600 x 600 DPI)

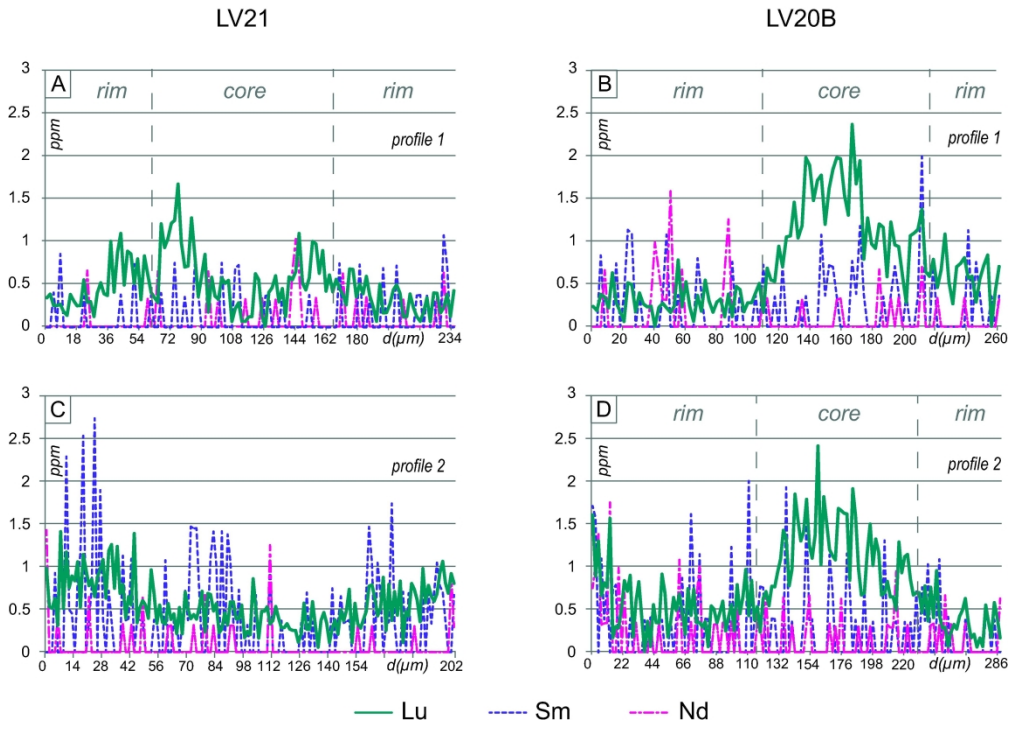

Figure 8: Trace element profiles for garnet from samples LV21 (a, c) and LV20B (b, d).

175x126mm (600 x 600 DPI)

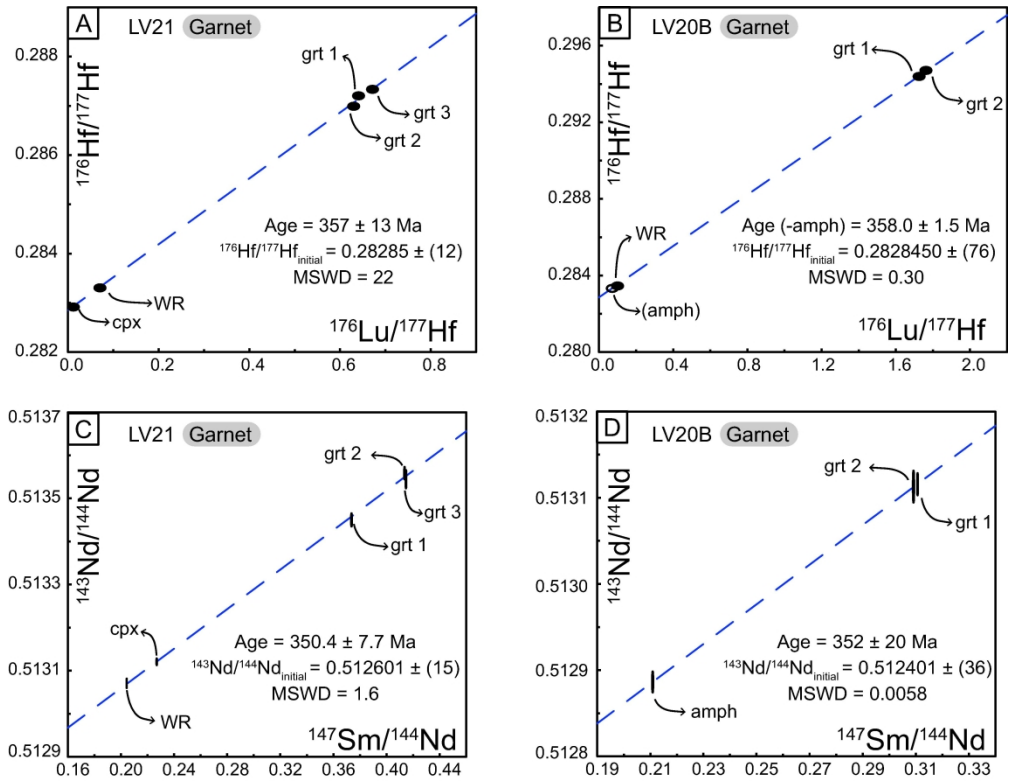

Figure 9: Lu–Hf (a, b) and Sm–Nd (c, d) isochron diagrams for samples LV21 and LV20B. WR – whole rock, grt – garnet, 1-3 – garnet fractions, amph – amphibole, cpx – clinopyroxene. Errors of Lu-Hf analyses were too small to be visible, consequently data points were increased.

170x132mm (600 x 600 DPI)

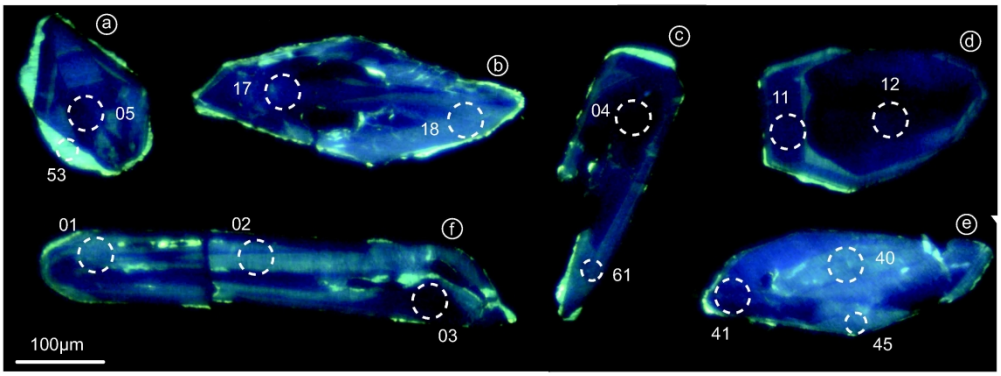

Figure 10: Selected cathodoluminescence images of zircon crystals, displaying the various textures observed. White (35 and 25 µm) circles show the location of the U-Pb analyses and the corresponding analysis number.

154x57mm (600 x 600 DPI)

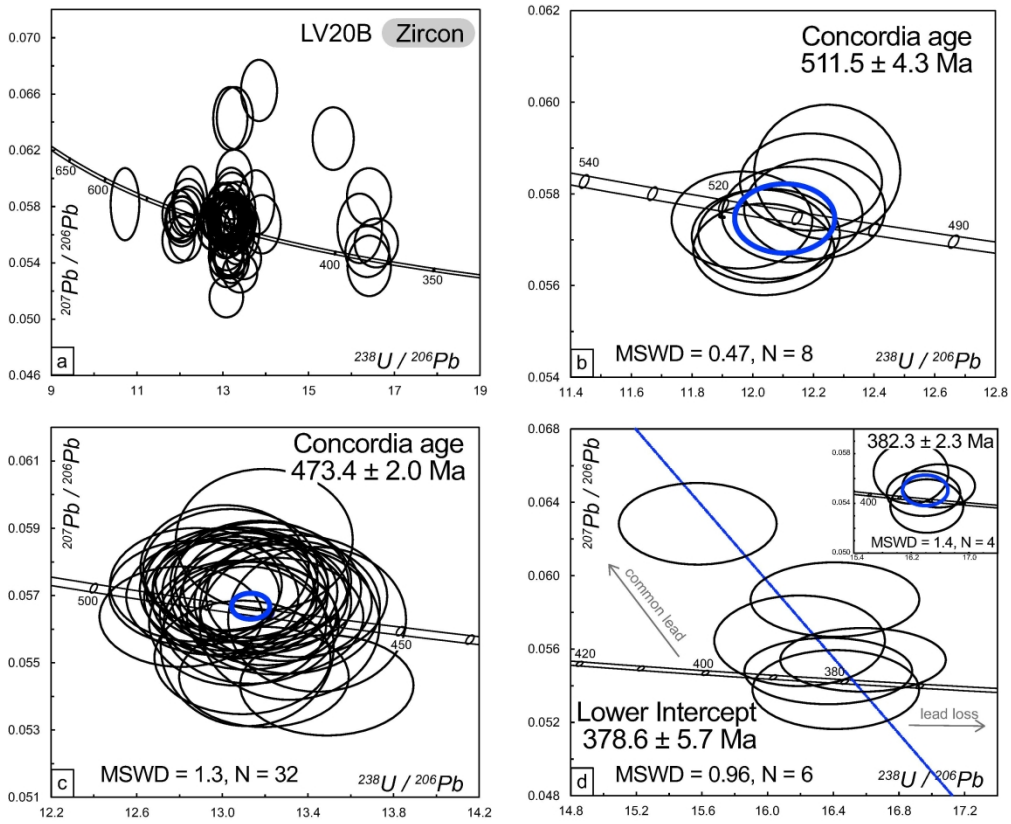

Figure 11: Tera–Wasserburg (207Pb/206Pb vs. 238U/206Pb) diagrams displaying all dates obtained on zircon (a), concordant Cambrian analyses (b), concordant Ordovician analyses (c), and all Devonian analyses with the Concordia age in insert (d).

142x116mm (600 x 600 DPI)

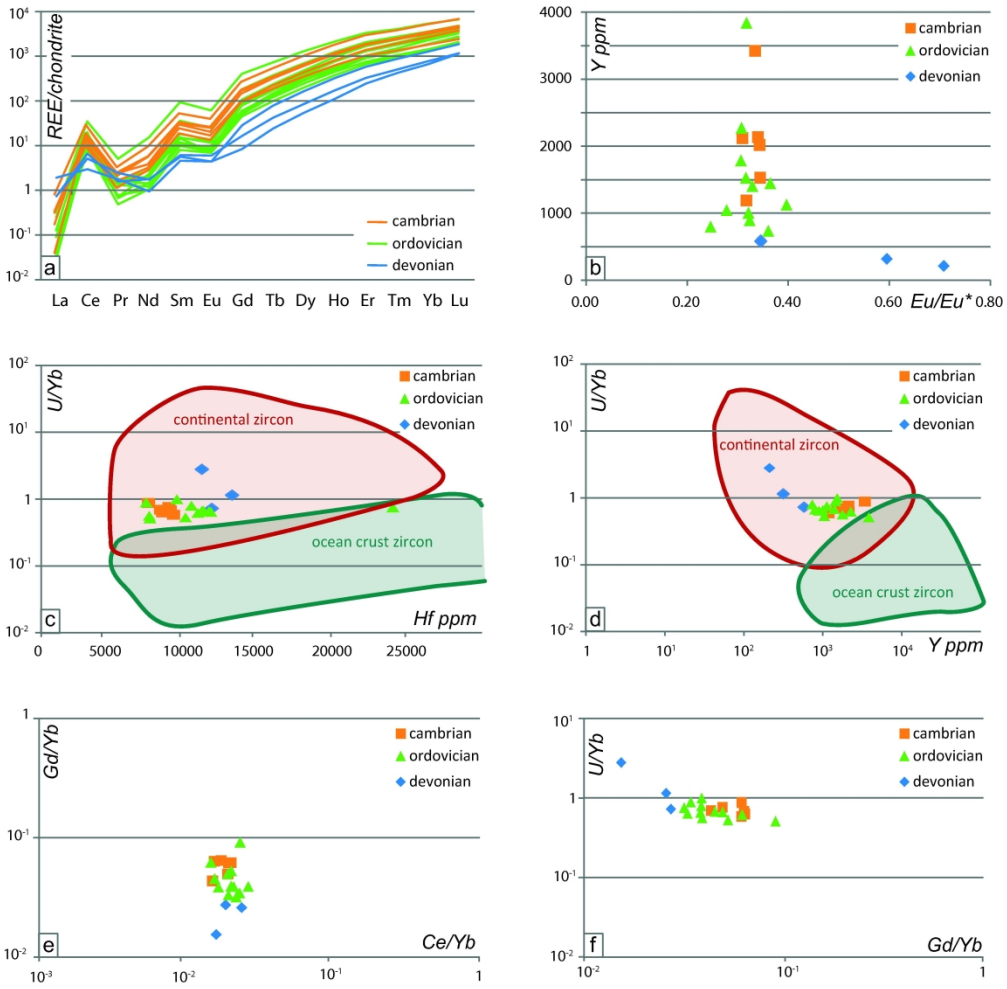

Figure 12: Trace element chemistry for dated zircons. (a) REE content normalized to chondrite for zircon displaying Devonian dates (blue), Ordovician dates (green), Cambrian dates (orange). (b) Y (ppm) vs. Eu/Eu* anomaly diagram, with the recorded dates colour-coded accordingly. (c) U/Yb vs. Hf and (d) U/Yb vs. Y discriminant geotectonic diagrams (Grimes et al., 2007). (e) Gd/Yb vs. Ce/Yb and (f) U/Yb vs. Gd/Yb petrogenetic diagram for zircon (Grimes et al., 2015). See text for details.

180x179mm (600 x 600 DPI)

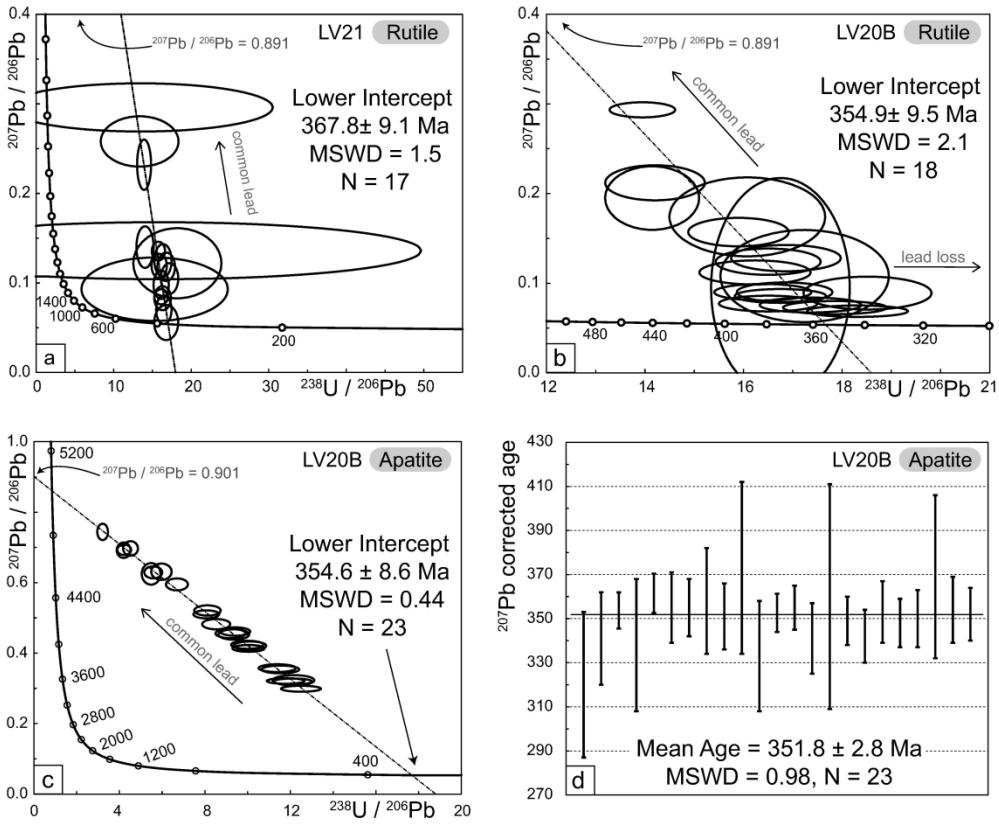

Figure 13: Tera–Wasserburg (207Pb/206Pb vs. 238U/206Pb) diagram displaying all dates obtained on rutile from LV21 (a) and LV20B (b) and apatite from LV20B (c) and the mean age 207Pb-corrected (d).

172x141mm (600 x 600 DPI)

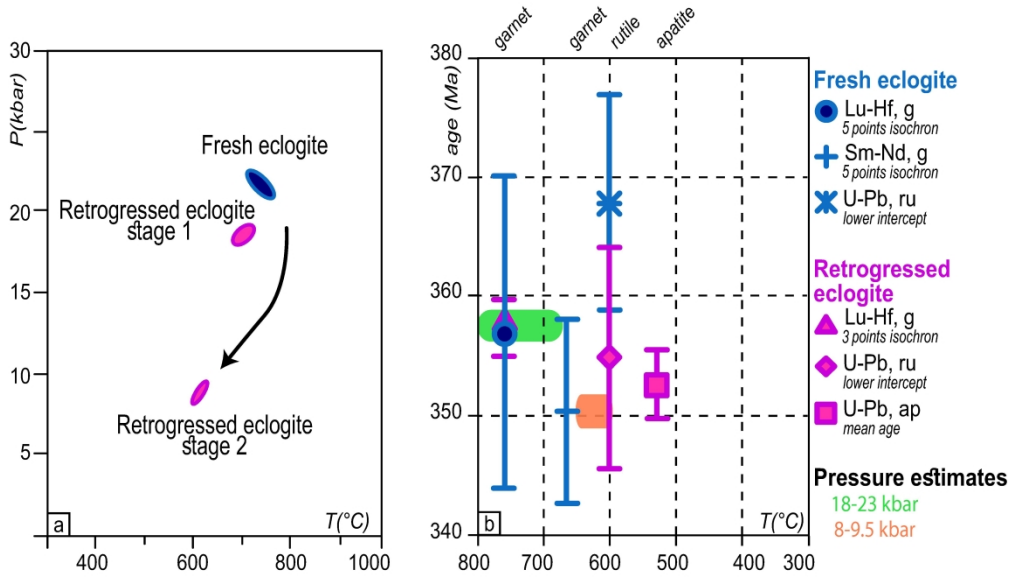

Figure 14: P–T (a) and Age – Temperature (b) diagram summarizing the chronological and petrological results from this study.

202x116mm (600 x 600 DPI)

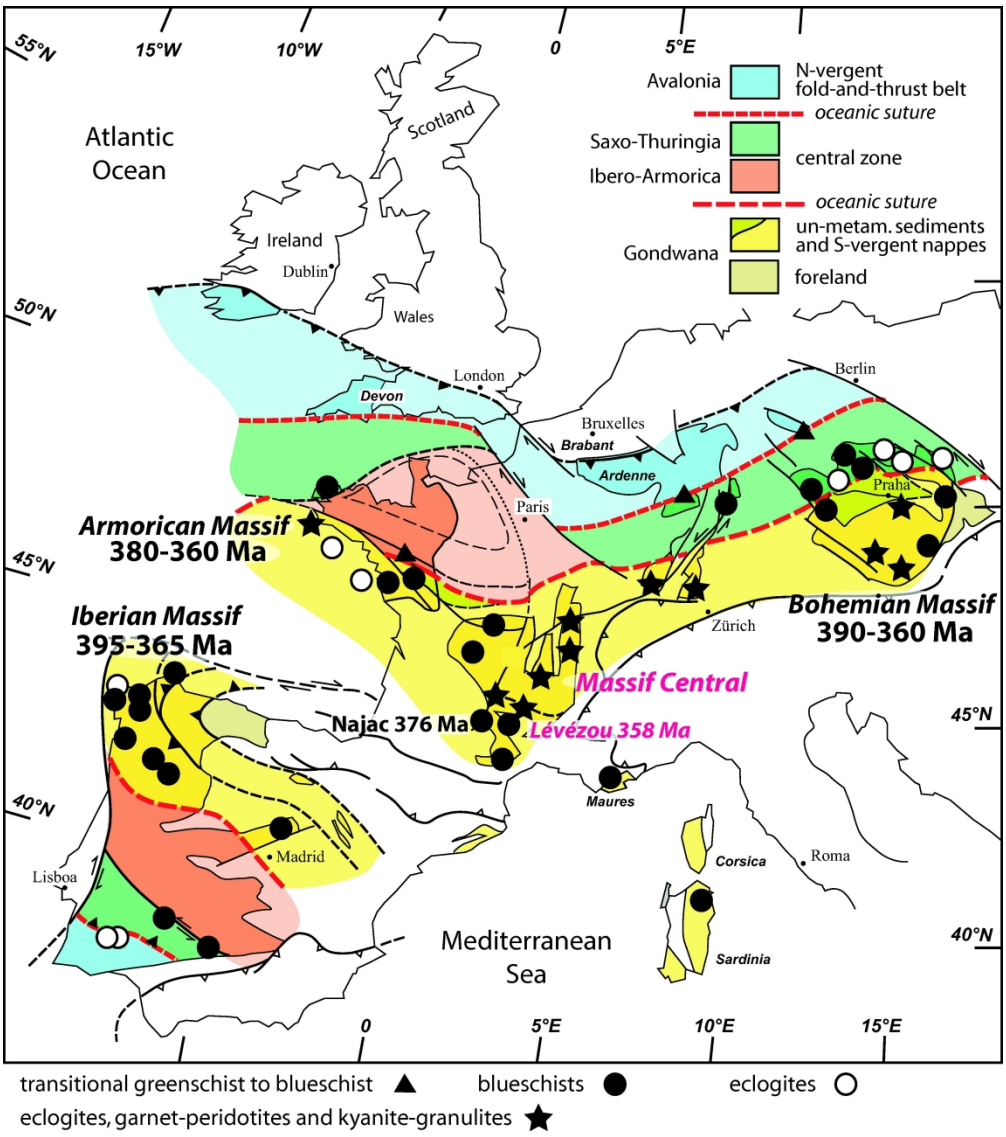

Figure 15: Ages of high-pressure metamorphic rocks in the European Variscan belt, (modified after Paquette et al., 2017). Result from this study is highlighted.

152x171mm (600 x 600 DPI)

Table 1 : Summary of the Lu–Hf and Sm–Nd dating results.

fraction	Weight [mg]	Sm [ppm]	Nd [ppm]	$^{147}Sm/^{144}Nd$	2se	$^{143}Nd/^{144}Nd$	2se	Lu [ppm]	Hf [ppm]	$^{176}Lu/^{177}Hf$	2se	$^{176}Hf/^{177}Hf$	2se
Sample LV21													
G1	73.83	0.6908	1.1180	0.3736	0.000271	0.513450	0.000012	0.592	0.131	0.642	0.0032	0.287209	0.000019
G2	70.93	0.6516	0.9528	0.4136	0.000184	0.513559	0.000012	0.598	0.135	0.629	0.0031	0.286990	0.000016
G3	52.72	0.6314	0.9209	0.4146	0.000190	0.513545	0.000017	0.593	0.125	0.670	0.0034	0.287331	0.000029
cpx	67.84	1.6321	4.3493	0.2269	0.000155	0.513121	0.000006	0.028	0.531	0.007	0.0000	0.282911	0.000007
WR	101.68	1.9344	5.7249	0.2043	0.000027	0.513071	0.000009	0.225	0.453	0.070	0.0004	0.283310	0.000006
Sample LV20B													
G1	68.54	0.6379	1.2416	0.3107	0.000107	0.513116	0.000011	0.924	0.075	1.737	0.0087	0.294480	0.000026
G2	65.09	0.6018	1.1771	0.3091	0.000170	0.513113	0.000015	1.269	0.102	1.755	0.0088	0.294631	0.000041
amph	66.78	1.6609	4.7618	0.2109	0.000157	0.512886	0.000010	0.348	0.683	0.072	0.0004	0.283362	0.000009
WR	102.66	2.7591	8.9256	0.1869	0.000040	0.512815	0.000005	0.358	0.643	0.079	0.0004	0.283374	0.000007